

# Hygro-thermo-mechanical analysis of spalling in concrete walls at high temperatures as a moving boundary problem

Michal Beneš and Radek Štefan

Faculty of Civil Engineering, Czech Technical University in Prague, Thákurova 7,  
166 29 Prague 6, Czech Republic

E-mail: radek.stefan@fsv.cvut.cz

**Abstract.** A mathematical model allowing coupled hygro-thermo-mechanical analysis of spalling in concrete walls at high temperatures by means of the moving boundary problem is presented. A simplified mechanical approach to account for effects of thermal stresses and pore pressure build-up on spalling is incorporated into the model. The numerical algorithm based on finite element discretization in space and the semi-implicit method for discretization in time is presented. The validity of the developed model is carefully examined by a comparison between experimental tests performed by Kalifa *et al.* [35] and Mindeguia [42] on concrete prismatic specimens under unidirectional heating of temperature of 600 °C and ISO 834 fire curve and the results obtained from the numerical model.

## 1. Introduction

Modelling and simulation of hygro-thermo-mechanical processes in rapidly heated concrete plays a significant role in the assessment of the load-bearing capacity and reliability of concrete structures. The impact of the increased pressures in pores and large temperature gradients cause explosive surface spalling leading to catastrophic service failures. Let us mention examples including fires in tunnels [50], nuclear reactor accidents [51] or damage of airfield concrete pavements due to high-temperature exhaust gas from aircraft engines during their take-off and landing procedures [33]. Several models based on more or less general physical background have been developed to simulate transport processes in heated concrete, see [27] and references therein. All developed models build on a system of conservation of mass and energy, but differ in the complexity of phase description of state of pore water as well as chemical reactions and different physical mechanisms of coupled transport processes in a pore system. A descriptive phenomenological approach was used to explore hygro-thermal processes in concrete exposed to temperatures exceeding 100 °C starting with the Bažant & Thonguthai models [7]. Here, the liquid water and water vapour are treated as a single phase, moisture, and the evaporable water is assumed to be formed by the capillary water only. The main advantages for usage of this approach is relative simplicity and small number of parameters that can be obtained from experiments. However, in such a way it is impossible to consider the effects of phase changes of water and the applicability of the single-fluid-phase models for temperatures above the critical point of water is disputed. These deficiencies led to the development of more detailed multi-phase description, see e.g. the works of Gawin *et al.* [21], Davie *et al.* [15] for specific examples. Coupled multi-phase models reflect the multi-phase structure of concrete, interactions between phases, phase changes of fluids and solids and non-linear couplings between thermal, hygral and mechanical processes. However, such increase in complexity comes at the expense of a large number of model parameters, which determination can be hardly obtained directly from experiments. Moreover, multi-phase models are computationally expansive. Despite rapid progress in computer technologies, complex models still exceed capabilities of recently developed numerical algorithms and computational hardware. Therefore, in this paper we will adopt a pragmatic concept and consider the simplified model obtained directly from the complex multi-phase description. Relative importance of thermodynamic fluxes will be quantitatively evaluated at the level of material point and these results will allow us to neglect less important transport phenomena without loss of capability to realistically predict behavior of concrete at extremely high temperatures.

Rapid external heating of concrete may lead to threat its stability due to concrete spalling. It is generally accepted that the spalling process in rapidly heated concrete is caused by two main processes – increase of pore pressure and development of thermal stresses – that may act separately or, which is more likely, in a combined way (see e.g. [37, Section 4]).

In literature, we can find many criteria to assess the risk and, in some cases, also the amount of concrete spalling (for a brief summary of some of these criteria, see e.g. [25, 37]). In our previous work [9], we have employed a heuristic engineering approach, originally proposed by [17, Section 3.3], in which the spalling is supposed to occur if the effective pore pressure exceeds the temperature dependent tensile strength of concrete. In the present paper, we extend this criterion in order to take into account not only the pore pressure (which seems to be not the dominant mechanism of spalling, as observed by recent experimental investigations [31, 43] and numerical simulations [45]) but also the thermal stress as a driving force of spalling.

The paper is organized as follows. In Section 2, we specify general thermodynamical and mechanical assumptions on concrete as a porous multi-phase medium to obtain a reasonably simple but still realistic model to predict hygro-thermal behavior of concrete at very high temperatures. This Section is concluded by presentation of conservation of mass and thermal energy, carefully derived in Appendix A by quantitative parameter analysis. In Sections 3 and 4, constitutive relationships are discussed in details and suitable boundary conditions for description of transport processes through the surfaces of the concrete wall are presented, respectively. Section 5 deals with the problem of moving boundary for spalling simulation. Our approach is based on the combined effect of pore pressure and thermal stresses in concrete under high temperature exposure. In Section 6, the complex problem is formulated as a fully coupled system of highly nonlinear partial differential equations (PDE's) supplemented with appropriate boundary and initial conditions. Based on the full FEM (in space) and semi-implicit (in time) discretization of the mentioned system of PDE's, an in-house research MATLAB code has been developed for the solution of the system of nonlinear algebraic equations. The numerical algorithm is presented in Section 7. Section 8 brings the complete list of material properties of moist concrete at high temperatures used in the numerical model. Section 9 is the key part of the paper. Here we present validation of the model by comparison of the numerical results with experiments reported in literature by means of three examples. First two examples, performed by Kalifa *et al.* [35] and, more recently, Mindeguia [42], examine the comparison of the measurements of pore pressure and temperature distributions with the predicted numerical simulations based on the present model under specific conditions excluding spalling phenomena. Finally, we apply the present model to investigate the surface spalling of high strength concrete prismatic specimen under unidirectional heating by the ISO 834 fire curve and compare the numerical results with experimental observations reported by Mindeguia [42, 43]. The summary of the outcomes achieved in this paper as well as the general conclusions and recommendations for future research appear in Section 10.

## 2. Basic conservation equations

### 2.1. General assumptions

A number of assumptions have been adopted to develop the coupled hygro-thermo-mechanical model for concrete spalling due to high temperatures exposure. Some of them of particular interest are as follows:

- (i) concrete is treated as a multi-phase system consisting of different phases and components: solid skeleton (composed of various chemical compounds and chemically bound water), liquid phase (combined capillary and adsorbed water), gas phase (a mixture of dry air and water vapour);
- (ii) the diffusive mass flux of water vapour is neglected and the diffusion of adsorbed water along the surface of the solid skeleton is considered through the liquid water relative permeability term,  $K_L$ , and is not therefore treated separately (see [15]);
- (iii) the effects of variations of pressure of dry air is ignored in the analysis. The mass of dry air in concrete is considered to be much smaller than the mass of liquid water and vapour and, consequently, the vapour pressure plays the crucial role (when compared to dry air) in spalling phenomena;
- (iv) above the critical point of water, only the vapour contribution to the mass transport is taken into account;
- (v) the spalling of concrete in a heated wall is assumed to be caused by a combination of the hygro-thermal stress due to the pore pressure build-up and the thermo-mechanical stress resulting from the restrained thermal dilatation;
- (vi) the wall is considered as fully mechanically restrained in the plane perpendicular to the wall thickness;
- (vii) the stresses resulting from the external mechanical load as well as the self-weight of the wall are not accounted for since their effect on the potential spalling may be considered to be negligible compared with the effect of mechanical restraint;
- (viii) the hygro-thermal and mechanical analysis is solved as a coupled problem.

### 2.2. Conservation laws

The mathematical model of moisture and heat transfer in concrete consists of the balance equations governing the conservation of mass (moisture) and thermal energy (cf. equations (??) and (??)).

*The mass balance equation of moisture (liquid water and vapour):*

$$\frac{\partial}{\partial t}(\eta_w \rho_w + \eta_v \rho_v) + \frac{\partial}{\partial x}(\eta_w \rho_w v_w + \eta_v \rho_v v_v) = \frac{\partial m_d}{\partial t}; \quad (1)$$

*energy conservation equation for moist concrete as the multi-phase system:*

$$(\rho c_p) \frac{\partial \theta}{\partial t} = -\frac{\partial q_c}{\partial x} - (\rho c_p v) \frac{\partial \theta}{\partial x} - \frac{\partial m_e}{\partial t} h_e - \frac{\partial m_d}{\partial t} h_d, \quad (2)$$

where

$$(\rho c_p) = c_p^w \rho_w \eta_w + c_p^g \rho_g \eta_g + c_p^s \rho_s \eta_s, \quad (3)$$

$$(\rho c_p v) = c_p^w \rho_w \eta_w v_w + c_p^g \rho_g \eta_g v_g \quad (4)$$

and  $c_p^g \rho_g = c_p^v \rho_v + c_p^a \rho_a$ . Governing equations (1) and (2) are carefully derived in Appendix A and the meanings of all symbols are explained in a well arranged way in Appendix B. It should be underlined that material coefficients of concrete and fluids that appear in governing equations (1) and (2) depend in non-linear manner upon the primary unknowns – temperature and pore pressure, which completely describe the state of concrete under thermal loading.

### 3. Constitutive relationships

Balance equations (1) and (2) are supplemented by an appropriate set of constitutive equations.

*Moisture flux.* As the constitutive equations for fluxes of fluid phases (liquid water and vapour) the *Darcy's law* is applied

$$\eta_w \rho_w v_w = - \rho_w \frac{K K_{rw}}{\mu_w} \frac{\partial P_L}{\partial x}, \quad P_L = P - P_c, \quad (5)$$

$$\eta_v \rho_v v_v = - \rho_v \frac{K K_{rg}}{\mu_g} \frac{\partial P}{\partial x}, \quad (6)$$

where  $P_L$  [Pa] is the pressure of liquid water,  $P_c$  [Pa] is the capillary pressure and  $P$  [Pa] represents the pore pressure due to the water vapour. Further,  $K$  [m<sup>2</sup>] represents the intrinsic permeability,  $K_{rw}$  [–] and  $K_{rg}$  [–] are the relative permeability of liquid water and relative permeability of gas,  $\mu_w$  [Pa s] and  $\mu_g$  [Pa s] represent the liquid water and gas dynamic viscosity.

The equilibrium state of the capillary water with the water vapour is expressed in the form of the *Kelvin equation*

$$P_c = -\rho_w \frac{\theta R}{M_w} \ln \left( \frac{P}{P_s} \right), \quad (7)$$

where  $P_c$  denotes the capillary pressure and the water vapour saturation pressure  $P_s$  [Pa] can be calculated from the following formula as a function of temperature  $\theta$  [K]

$$P_s(\theta) = \exp \left( 23,5771 - \frac{4042,9}{\theta - 37,58} \right). \quad (8)$$

Water vapour is considered to behave as perfect gas, therefore, *Clapeyron equation* [21]

$$\rho_v = \frac{P M_w}{\theta R} \quad (9)$$

is assumed as the state equation, where  $R$  [J mol<sup>-1</sup> K<sup>-1</sup>] is the gas constant (8.3145 J mol<sup>-1</sup> K<sup>-1</sup>) and  $M_w$  [kg mol<sup>-1</sup>] represents molar mass of water vapour.

*Heat flux.* For the heat flux induced by conduction the Fourier's law is applied in the form

$$q_c = -\lambda_c \frac{\partial \theta}{\partial x}, \quad (10)$$

where  $\lambda_c$  [ $\text{W m}^{-1} \text{K}^{-1}$ ] represents the temperature and saturation dependent effective thermal conductivity of moist concrete.

*Evaporation.* In order to determine the amount of heat due to evaporation or, reversely, condensation processes, the water vapour conservation equation

$$\frac{\partial(\eta_v \rho_v)}{\partial t} + \frac{\partial(\eta_v \rho_v v_v)}{\partial x} = \frac{\partial m_e}{\partial t} \quad (11)$$

needs to be incorporated into the energy conservation equation (2) which will be handled in Section 6.2.

*Dehydration.* Following [13, 19], the evolution of mass source term  $m_d$  [ $\text{kg m}^{-3} \text{s}^{-1}$ ] related to the dehydration process is considered through the following evolution law

$$\frac{\partial m_d}{\partial t} = -\frac{1}{\tau}(m_d - m_{d,eq}(\theta)), \quad (12)$$

where  $m_{d,eq}$  [ $\text{kg m}^{-3} \text{s}^{-1}$ ] is the mass of water released at the equilibrium according to temperature  $\theta$  and  $\tau$  [s] is the characteristic time of mass loss governing the asymptotic evolution of the dehydration process.

#### 4. Boundary conditions

To describe coupled transport processes through the surfaces of the wall, one should prescribe the appropriate boundary conditions across the boundary. Homogeneous Neumann conditions

$$h_e \rho_v \eta_v v_v - \lambda_c \frac{\partial \theta}{\partial x} = 0, \quad (13)$$

$$\rho_w \eta_w v_w + \rho_v \eta_v v_v = 0 \quad (14)$$

are usually applied on the insulated surface of the wall. Boundary conditions of the form

$$\left( h_e \rho_v \eta_v v_v - \lambda_c \frac{\partial \theta}{\partial x} \right) n_x = \alpha_c (\theta - \theta_\infty) + \epsilon \sigma_{SB} (\theta^4 - \theta_\infty^4), \quad (15)$$

$$(\rho_w \eta_w v_w + \rho_v \eta_v v_v) n_x = \beta_c (\rho_v - \rho_{v\infty}) \quad (16)$$

( $n_x = \pm 1$ ) are of importance on the exposed side of the wall, where the terms on the right hand side of (15) represent the heat energy dissipated by convection and radiation to the surrounding medium and the term on the right hand side of (16) represents a water vapour dissipated into the surrounding medium.

## 5. Moving boundary for spalling simulation in concrete walls

### 5.1. Spalling criterion

Let us assume a concrete wall of a thickness  $\ell$  exposed to fire on boundary  $x = \ell$ . The spalling at position  $x \in (0, \ell)$  and time  $t$  occurs if (cf. [45, p. 613], [48, Section 2.3])

$$F(f_c(\theta), f_t(\theta), \sigma_{ht}(P, \theta), \sigma_{tm}(\theta)) > 1, \quad (17)$$

where  $F$  is a dimensionless failure parameter (failure function),  $f_c$  and  $f_t$  are the temperature dependent uniaxial compressive and tensile strengths of concrete, respectively,  $\sigma_{ht}$  and  $\sigma_{tm}$  are the actual stresses in concrete caused by hygro-thermal and thermo-mechanical processes, respectively, and  $P$  and  $\theta$  are the pore pressure and temperature in concrete at position  $x$  and time  $t$ , respectively.

Note that the strengths of concrete (both compressive and tensile) are assumed to be positive values while the strains and stresses are taken as positive in tension and negative in compression.

### 5.2. Hygro-thermal stress

Hygro-thermal stress in heated concrete is a tensile stress caused by the pore pressure build-up. There are several approaches to determine the hygro-thermal stress. These approaches may differ both in the definition of the pore pressure and also in the manner in which the pore pressure is converted into the hygro-thermal stress. The pore pressure may be assumed to be equal to the vapour pressure (e.g. [17]), to the gas pressure, or can be calculated as the Bishop's stress [14, 21, 45, 48]. The hygro-thermal stress (i.e. the effective pore pressure) can be determined from the pore pressure by the hollow spherical model [30], or multiplying respectively by a Biot's coefficient [45, 48] or by a concrete porosity [17].

Here, we adopt the approach proposed by [17], in which

$$\sigma_{ht}(P, \theta) = P\phi(\theta), \quad (18)$$

where  $P$  is the pore pressure due to water vapour and  $\phi$  is the temperature dependent concrete porosity.

### 5.3. Thermo-mechanical stress

The thermo-mechanical stress in a heated concrete wall generally depends on the external mechanical load applied on the wall, on its geometry (wall thickness, load eccentricity), material properties (both hygro-thermal and mechanical), and boundary conditions (heating, mechanical restraint).

In our approach, we follow a conservative assumption, also adopted by e.g. [45, 55], in which the wall is supposed to be fully mechanically restrained in the plane perpendicular to the wall thickness. On the other hand, the stresses resulting from the external mechanical load as well as the self-weight of the wall are not accounted for since

their effect on the potential spalling may be considered to be negligible when compared with the effect of mechanical restraint (cf. [45, 55]).

In order to assess the thermal stress arising from the mechanical restraint, we have to focus on the stress-strain conditions in the heated wall. It is widely accepted that the total strain in concrete subjected to high temperatures may be decomposed into several parts which differ in their physical meaning. Hence, we can write [5, eq. (4.2)], [4, eq. (1)], [39, eq. (1)]

$$\epsilon_{tot} = \epsilon_{\theta}(\theta) + \epsilon_{\sigma}(\sigma, \theta) + \epsilon_{cr}(\sigma, \theta, t) + \epsilon_{tr}(\sigma, \theta), \quad (19)$$

where  $\epsilon_{tot}$  is the total strain,  $\epsilon_{\theta}$  is the free thermal strain,  $\epsilon_{\sigma}$  is the instantaneous stress-related strain (which can be divided into the elastic part and the plastic part,  $\epsilon_e$  and  $\epsilon_p$ , respectively, see e.g. [10]),  $\epsilon_{cr}$  is the creep strain,  $\epsilon_{tr}$  is the transient strain,  $\sigma$  is the stress, and  $t$  is the time.

As stated in e.g. [28], the creep strain,  $\epsilon_{cr}$ , is usually neglected. Moreover, the stress-dependent strains can be assumed together (with or without  $\epsilon_{\sigma}$  or  $\epsilon_{cr}$ ) as the mechanical strain (see [28]) or as the so called load induced thermal strain – LITS (see e.g. [4, 38, 53, 55]).

Here, we adopt a constitutive law proposed by Eurocode 2 [2], in which the stress is expressed in terms of the total mechanical strain,  $\epsilon_m$ , that includes the transient strain implicitly, while the creep strain is omitted [4, 11, 28], and hence, we can write

$$\epsilon_{tot} = \epsilon_{\theta}(\theta) + \epsilon_m(\sigma, \theta). \quad (20)$$

Since the wall is supposed to be fully mechanically restrained, the total strain is equal to zero and the mechanical strain can be expressed as

$$\epsilon_m = -\epsilon_{\theta}(\theta). \quad (21)$$

As mentioned above, the constitutive law given by Eurocode 2 [2] has the form

$$\sigma = \mathcal{L}(\epsilon_m, \theta). \quad (22)$$

In our case (see equation (21)), the stress can be expressed directly as a function of temperature (the formulas provided by Eurocode 2 [2] for  $\epsilon_{\theta}(\theta)$  and  $\mathcal{L}(\epsilon_m, \theta)$  are stated in Section 8). It should be noted that the stress in concrete determined by (22) belongs to the uniaxial conditions. For the plane stress conditions, we get

$$\sigma_{tm}(\theta) = \frac{1}{1 - \nu(\theta)} \sigma(\theta), \quad (23)$$

where  $\nu$  is the Poisson's ratio (see Section 8), and  $\sigma$  is the uniaxial stress given by (22) (with  $\epsilon_m$  determined by (21)).

#### 5.4. Resulting stress conditions

Let us assume that the wall thickness,  $\ell$ , which is much smaller than the other dimensions of the wall, is parallel to the  $x$ -axis, and the wall surfaces (at positions of  $x = 0$  and  $x = \ell$ ) are parallel to the plane  $y$ - $z$  (cf. [45]). As mentioned above and as stated in



and  $\xi$ ,  $\rho$  and  $\vartheta$  are the Haigh–Westergaard coordinates (see e.g. [32, 41]).

The Men etrey–Willam failure function for the plane stress conditions (i.e. for  $\sigma_3 = 0$ ) is shown in Figure 2.

In our case, in which  $\sigma_1 = \sigma_{ht}$  and  $\sigma_2 = \sigma_3 = \sigma_{tm}$ , we can write

$$\xi = \frac{1}{\sqrt{3}}(\sigma_{ht} + 2\sigma_{tm}), \quad (28)$$

$$\rho = \sqrt{\frac{2}{3}}(\sigma_{ht} - \sigma_{tm}), \quad (29)$$

$$\cos(3\vartheta) = \frac{\sigma_{ht} - \sigma_{tm}}{\sqrt{(\sigma_{ht} - \sigma_{tm})^2}}. \quad (30)$$

Since  $\sigma_{tm} \leq 0 < \sigma_{ht}$ , and  $0.5 < e_F \leq 1.0$ , it is obvious that  $\vartheta = 0$ , and  $r = 1/e_F$ . Substituting this in (26) and assuming the strengths of concrete as temperature dependent, we get the resulting failure function used in our model (cf. [45, p. 613])

$$F = \left( \frac{\sigma_{ht}(P, \theta) - \sigma_{tm}(\theta)}{f_c(\theta)} \right)^2 + \frac{f_c(\theta)^2 - f_t(\theta)^2}{f_c(\theta)^2 f_t(\theta)} \left( \sigma_{ht}(P, \theta) + \frac{2e_F - 1}{e_F + 1} \sigma_{tm}(\theta) \right), \quad (31)$$

which is illustrated in Figure 3.

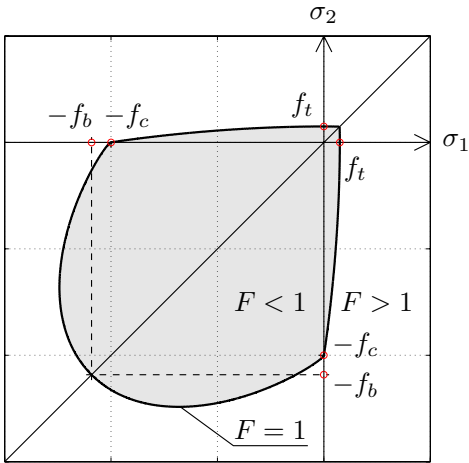


**Figure 2.** Men etrey–Willam [41] failure function

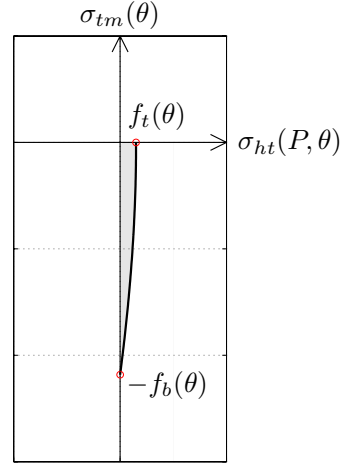


**Figure 3.** Failure function used in our model

### 5.5. Evolution law for moving boundary due to spalling

In our regularized approach, the instantaneous spalling of concrete is approximated by rapid continuous process in such a way that sheet of concrete is continuously removed from the wall and the receding outer surface forms the moving boundary. In general, in one dimension, the external loading to the concrete wall according to the boundary

conditions (15) and (16) is prescribed on the unknown ablating boundary  $x = \ell(t)$ . For the spalling of the wall originally occupying the space  $0 \leq x \leq \ell_0$ , we propose the governing equation of the form

$$\frac{d\ell}{dt} = -\frac{\ell}{\gamma} [\max(F) - 1]^+, \quad \ell(0) = \ell_0, \quad (32)$$

where the position of the moving boundary  $\ell$  has to be determined as a part of the solution. Further,  $x^+ = \max(0, x)$ ,  $\gamma$  [s] represents the characteristic time of spalling process and  $\max(F)$  is the maximal value of failure function (31) achieved within the wall  $(0, \ell)$  at actual time  $t$ .

## 6. Formulation of the problem

### 6.1. Modification of mass balance equation

Let us start with modification of the equation (1). Denote by  $m = \eta_w \rho_w + \eta_v \rho_v$  the total mass of moisture (including liquid water and vapour). Incorporating the constitutive relations (5) and (6) into the mass balance equation (1) yields

$$\frac{\partial m}{\partial t} = \frac{\partial}{\partial x} \left[ \left( \rho_w \frac{K K_{rw}}{\mu_w} + \rho_v \frac{K K_{rg}}{\mu_g} \right) \frac{\partial P}{\partial x} - \rho_w \frac{K K_{rw}}{\mu_w} \frac{\partial P_c}{\partial x} \right] + \frac{\partial m_d}{\partial t}. \quad (33)$$

Here  $P_c = P_c(P, \theta)$  via equation (7). After additional modification, the equation (33) can be written in a general form

$$\frac{\partial m}{\partial t} - \frac{\partial m_d}{\partial t} = \frac{\partial}{\partial x} \left( K_{mP} \frac{\partial P}{\partial x} + K_{m\theta} \frac{\partial \theta}{\partial x} \right), \quad (34)$$

where

$$K_{mP} = \rho_w \frac{K K_{rw}}{\mu_w} \left( 1 - \frac{\partial P_c}{\partial P} \right) + \rho_v \frac{K K_{rg}}{\mu_g}, \quad (35)$$

$$K_{m\theta} = -\rho_w \frac{K K_{rw}}{\mu_w} \frac{\partial P_c}{\partial \theta}. \quad (36)$$

### 6.2. Modification of energy conservation equation

Incorporating water vapour conservation equation into the term corresponding to the latent heat of evaporation leads to the following modified energy balance equation

$$\begin{aligned} & (\rho c_p) \frac{\partial \theta}{\partial t} + h_e \frac{\partial (\eta_v \rho_v)}{\partial t} + h_d \frac{\partial m_d}{\partial t} \\ & = \frac{\partial}{\partial x} \left( \lambda_c \frac{\partial \theta}{\partial x} \right) - h_e \frac{\partial (\eta_v \rho_v v_v)}{\partial x} - (c_p^w \rho_w \eta_w v_w + c_p^g \rho_g \eta_g v_g) \frac{\partial \theta}{\partial x}. \end{aligned} \quad (37)$$

Simple calculation yields

$$\begin{aligned} h_e \frac{\partial (\eta_v \rho_v v_v)}{\partial x} & = \frac{\partial (h_e \eta_v \rho_v v_v)}{\partial x} - (\eta_v \rho_v v_v) \frac{\partial h_e}{\partial x} \\ & = -\frac{\partial}{\partial x} \left( h_e \rho_v \frac{K K_{rg}}{\mu_g} \frac{\partial P}{\partial x} \right) + \rho_v \frac{K K_{rg}}{\mu_g} \frac{\partial h_e}{\partial \theta} \frac{\partial P}{\partial x} \frac{\partial \theta}{\partial x}. \end{aligned} \quad (38)$$

Incorporating the equation (38) into (37) reads

$$M_{\theta P} \frac{\partial P}{\partial t} + M_{\theta\theta} \frac{\partial \theta}{\partial t} + h_d \frac{\partial m_d}{\partial t} = \frac{\partial}{\partial x} \left( K_{\theta P} \frac{\partial P}{\partial x} + K_{\theta\theta} \frac{\partial \theta}{\partial x} \right) + \left( C_{\theta P} \frac{\partial P}{\partial x} + C_{\theta\theta} \frac{\partial \theta}{\partial x} \right) \frac{\partial \theta}{\partial x}, \quad (39)$$

where

$$M_{\theta P} = h_e \frac{\partial (\eta_v \rho_v)}{\partial P}, \quad (40)$$

$$M_{\theta\theta} = (\rho c_p) + h_e \frac{\partial (\eta_v \rho_v)}{\partial \theta}, \quad (41)$$

$$K_{\theta P} = h_e \rho_v \frac{K K_{rg}}{\mu_g}, \quad (42)$$

$$K_{\theta\theta} = \lambda_c, \quad (43)$$

$$C_{\theta P} = c_p^w \rho_w \frac{K K_{rw}}{\mu_w} \left( 1 - \frac{\partial P_c}{\partial P} \right) + \left( c_p^v - \frac{\partial h_e}{\partial \theta} \right) \rho_v \frac{K K_{rg}}{\mu_g}, \quad (44)$$

$$C_{\theta\theta} = -c_p^w \rho_w \frac{K K_{rw}}{\mu_w} \frac{\partial P_c}{\partial \theta}. \quad (45)$$

### 6.3. Resulting model

The full mathematical model consists of the balance equations for moisture and energy, state equation of pore water (moisture), governing equation for dehydration, evolution equation for moving boundary due to spalling, the set of appropriate boundary and initial conditions specifying the fields of pore pressure, temperature, mass of dehydrated water and initial thickness of the wall.

*Moisture conservation equation:*

$$\frac{\partial m}{\partial t} - \frac{\partial m_d}{\partial t} = \frac{\partial}{\partial x} \left( K_{mP} \frac{\partial P}{\partial x} + K_{m\theta} \frac{\partial \theta}{\partial x} \right); \quad (46)$$

*energy conservation equation:*

$$M_{\theta P} \frac{\partial P}{\partial t} + M_{\theta\theta} \frac{\partial \theta}{\partial t} + h_d \frac{\partial m_d}{\partial t} = \frac{\partial}{\partial x} \left( K_{\theta P} \frac{\partial P}{\partial x} + K_{\theta\theta} \frac{\partial \theta}{\partial x} \right) \quad (47)$$

$$+ \left( C_{\theta P} \frac{\partial P}{\partial x} + C_{\theta\theta} \frac{\partial \theta}{\partial x} \right) \frac{\partial \theta}{\partial x}; \quad (48)$$

*state equation of moisture:*

$$m = \eta_w \rho_w + \eta_v \rho_v; \quad (49)$$

*governing equation of dehydration:*

$$\frac{\partial m_d}{\partial t} = -\frac{1}{\tau} (m_d - m_{d,eq}(\theta)); \quad (50)$$

*evolution law for moving boundary due to spalling:*

$$\frac{d\ell}{dt} = -\frac{\ell}{\gamma} [\max(F) - 1]^+; \quad (51)$$

boundary conditions (at  $x = 0$  and  $x = \ell$ ):

$$-\left(K_{mP}\frac{\partial P}{\partial x} + K_{m\theta}\frac{\partial \theta}{\partial x}\right)n_x = \beta_c(\rho_v - \rho_{v\infty}), \quad (52)$$

$$-\left(K_{\theta P}\frac{\partial P}{\partial x} + K_{\theta\theta}\frac{\partial \theta}{\partial x}\right)n_x = \alpha_c(\theta - \theta_\infty) + e\sigma_{SB}(\theta^4 - \theta_\infty^4); \quad (53)$$

and initial conditions (at  $t = 0$ ):

$$P = P_0, \quad (54)$$

$$\theta = \theta_0, \quad (55)$$

$$\ell = \ell_0, \quad (56)$$

$$m_d = 0. \quad (57)$$

The unknowns in the model are the moisture content  $m$ , pore pressure  $P$ , temperature  $\theta$ , mass of dehydrated water  $m_d$  and the actual thickness of the wall  $\ell$ . Transport coefficients  $K_{mP}, K_{m\theta}, M_{\theta P}, M_{\theta\theta}, K_{\theta P}, K_{\theta\theta}, C_{\theta P}, C_{\theta\theta}$ , defined by (35) and (36) and (40)–(45), depend in non-linear manner upon temperature  $\theta$  and pressure  $P$ . Material non-linearities are described in detail in Section 8.

## 7. FEM formulation and solution strategy

Let  $0 = t_0 < t_1 < \dots < t_N = T$  be an equidistant partitioning of time interval  $[0, T]$  with step  $\Delta t$ . Set a fixed integer  $n$  such that  $0 \leq n < N$ . In what follows we abbreviate  $f(x, t_n)$  by  $f^n$  for any function  $f$ . The time discretization of the continuous model is accomplished through a semi-implicit difference scheme

$$\frac{m^{n+1} - m^n}{\Delta t} = \frac{\partial}{\partial x} \left( K_{mP}^n \frac{\partial P^{n+1}}{\partial x} + K_{m\theta}^n \frac{\partial \theta^{n+1}}{\partial x} \right) + \frac{m_d^{n+1} - m_d^n}{\Delta t}, \quad (58)$$

$$\begin{aligned} M_{\theta P}^n \frac{P^{n+1} - P^n}{\Delta t} + M_{\theta\theta}^n \frac{\theta^{n+1} - \theta^n}{\Delta t} &= \frac{\partial}{\partial x} \left( K_{\theta P}^n \frac{\partial P^{n+1}}{\partial x} + K_{\theta\theta}^n \frac{\partial \theta^{n+1}}{\partial x} \right) \\ &+ \left( C_{\theta P}^n \frac{\partial P^n}{\partial x} + C_{\theta\theta}^n \frac{\partial \theta^n}{\partial x} \right) \frac{\partial \theta^n}{\partial x} - h_d^n \frac{m_d^{n+1} - m_d^n}{\Delta t}, \end{aligned} \quad (59)$$

$$m^{n+1} = \eta_w^{n+1} \rho_w(\theta^{n+1}) + \eta_v^{n+1} \rho_v(\theta^{n+1}, P^{n+1}), \quad (60)$$

$$\frac{m_d^{n+1} - m_d^n}{\Delta t} = -\frac{1}{\tau} (m_d^n - m_{d,eq}(\theta^n)), \quad (61)$$

$$\frac{\ell^{n+1} - \ell^n}{\Delta t} = -\frac{\ell^{n+1}}{\gamma} [\max(F^n) - 1]^+, \quad (62)$$

$$\begin{aligned} -n_x \left( K_{mP}^n \frac{\partial P^{n+1}}{\partial x} + K_{m\theta}^n \frac{\partial \theta^{n+1}}{\partial x} \right) \Big|_{x=0, x=\ell^{n+1}} \\ = \beta_c (\rho_v(P^{n+1}, \theta^{n+1}) - \rho_v(P_\infty^{n+1}, \theta_\infty^{n+1})), \end{aligned} \quad (63)$$

$$\begin{aligned} -n_x \left( K_{\theta P}^n \frac{\partial P^{n+1}}{\partial x} + K_{\theta\theta}^n \frac{\partial \theta^{n+1}}{\partial x} \right) \Big|_{x=0, x=\ell^{n+1}} \\ = \alpha_c (\theta^{n+1} - \theta_\infty^{n+1}) + e\sigma_{SB} ((\theta^{n+1})^4 - (\theta_\infty^{n+1})^4), \end{aligned} \quad (64)$$

where  $\eta_w^{n+1} = \eta_w(\theta^{n+1}, P^{n+1})$  and  $\eta_v^{n+1} = \eta_v(\theta^{n+1}, P^{n+1})$ . Further,  $n_x = +1$  for  $x = \ell^{n+1}$  and  $n_x = -1$  for  $x = 0$ .

Applying the Galerkin procedure to the mass and energy conservation equations leads to the system of non-linear algebraic equations

$$\frac{1}{\Delta t} \mathbf{M}^n (\mathbf{x}^{n+1} - \mathbf{x}^n) + \mathbf{K}^n \mathbf{x}^{n+1} + \mathbf{f}^{n+1}(\mathbf{x}^{n+1}) = \mathbf{0}, \quad (65)$$

where  $\mathbf{x}^{n+1} = (\mathbf{m}^{n+1}, \theta^{n+1}, \mathbf{P}^{n+1})^T$ ,  $m^{n+1}(x) = \mathbf{N}(x)\mathbf{m}^{n+1}$ ,  $\theta^{n+1}(x) = \mathbf{N}(x)\theta^{n+1}$  and  $P^{n+1}(x) = \mathbf{N}(x)\mathbf{P}^{n+1}$ , stores the unknown nodal values of moisture, temperature and pore pressure at time  $t_{n+1}$ , respectively. The constant matrices in (65) exhibit a block structure

$$\mathbf{M}^n = \begin{bmatrix} \mathbf{M}_{mm}^n & \mathbf{0} & \mathbf{0} \\ \mathbf{0} & \mathbf{M}_{\theta\theta}^n & \mathbf{M}_{\theta P}^n \\ \mathbf{0} & \mathbf{0} & \mathbf{0} \end{bmatrix}, \quad \mathbf{K}^n = \begin{bmatrix} \mathbf{0} & \mathbf{K}_{m\theta}^n & \mathbf{K}_{mP}^n \\ \mathbf{0} & \mathbf{K}_{\theta\theta}^n & \mathbf{K}_{\theta P}^n \\ \mathbf{0} & \mathbf{0} & \mathbf{0} \end{bmatrix} \quad (66)$$

and the non-linear term reads as

$$\mathbf{f}^{n+1}(\mathbf{x}^{n+1}) = \begin{pmatrix} \mathbf{f}_m^{n+1}(\mathbf{x}^{n+1}) \\ \mathbf{f}_\theta^{n+1}(\mathbf{x}^{n+1}) \\ \mathbf{f}_P^{n+1}(\mathbf{x}^{n+1}) \end{pmatrix}. \quad (67)$$

The non-linear system (65) is solved iteratively using the Newton's method (see [49]).

The individual matrices  $\mathbf{M}_\bullet^n$  can be expressed as

$$\mathbf{M}_{mm}^n = \int_0^{\ell^{n+1}} \mathbf{N}(x)^\top \mathbf{N}(x) dx, \quad (68)$$

$$\mathbf{M}_{\theta\theta}^n = \int_0^{\ell^{n+1}} \mathbf{N}(x)^\top \left[ \left( (\rho c_p) + h_e \frac{\partial(\eta_v \rho_v)}{\partial \theta} \right) \mathbf{N}(x) \right] dx, \quad (69)$$

$$\mathbf{M}_{\theta P}^n = \int_0^{\ell^{n+1}} \mathbf{N}(x)^\top \left[ h_e \frac{\partial(\eta_v \rho_v)}{\partial P} \mathbf{N}(x) \right] dx, \quad (70)$$

whereas the blocks  $\mathbf{K}_\bullet^n$  attain the form

$$\mathbf{K}_{m\theta}^n = \int_0^{\ell^{n+1}} \left( \frac{\partial}{\partial x} \mathbf{N}(x) \right)^\top \left[ -\rho_w \frac{K K_{rw}}{\mu_w} \frac{\partial P_c}{\partial \theta} \frac{\partial}{\partial x} \mathbf{N}(x) \right] dx, \quad (71)$$

$$\mathbf{K}_{mP}^n = \int_0^{\ell^{n+1}} \left( \frac{\partial}{\partial x} \mathbf{N}(x) \right)^\top \left[ \left( \rho_w \frac{K K_{rw}}{\mu_w} \left( 1 - \frac{\partial P_c}{\partial P} \right) + \rho_v \frac{K K_{rg}}{\mu_g} \right) \frac{\partial}{\partial x} \mathbf{N}(x) \right] dx, \quad (72)$$

$$\mathbf{K}_{\theta\theta}^n = \int_0^{\ell^{n+1}} \left( \frac{\partial}{\partial x} \mathbf{N}(x) \right)^\top \left[ \lambda_c \frac{\partial}{\partial x} \mathbf{N}(x) \right] dx,$$

$$\mathbf{K}_{\theta P}^n = \int_0^{\ell^{n+1}} \left( \frac{\partial}{\partial x} \mathbf{N}(x) \right)^\top \left[ h_e \rho_v \frac{K K_{rg}}{\mu_g} \frac{\partial}{\partial x} \mathbf{N}(x) \right] dx. \quad (73)$$

The non-linear terms  $\mathbf{f}_\bullet^n$  are provided by

$$\begin{aligned} \mathbf{f}_m^{n+1}(\mathbf{x}^{n+1}) &= \int_0^{\ell^{n+1}} -\frac{m_d^{n+1} - m_d^n}{\Delta t} \mathbf{N}(x)^\top dx \\ &+ \left[ (\beta_c (\rho_v(P^{n+1}, \theta^{n+1}) - \rho_v(P_\infty^{n+1}, \theta_\infty^{n+1}))) \mathbf{N}(x)^\top \right]_{x=0}^{x=\ell^{n+1}}, \end{aligned} \quad (74)$$

$$\begin{aligned}
\mathbf{f}_\theta^{n+1}(\mathbf{x}^{n+1}) &= \int_0^{\ell^{n+1}} h_d^n \frac{m_d^{n+1} - m_d^n}{\Delta t} \mathbf{N}(x)^\top dx \\
&\quad - \int_0^{\ell^{n+1}} \left( C_{\theta P}^n \frac{\partial P^n}{\partial x} + C_{\theta\theta}^n \frac{\partial \theta^n}{\partial x} \right) \frac{\partial \theta^n}{\partial x} \mathbf{N}(x)^\top dx \\
&\quad + \left[ (\alpha_c(\theta^{n+1} - \theta_\infty^{n+1}) + e\sigma_{SB}((\theta^{n+1})^4 - (\theta_\infty^{n+1})^4)) \mathbf{N}(x)^\top \right]_{x=0}^{x=\ell^{n+1}}, \quad (75)
\end{aligned}$$

$$\begin{aligned}
\mathbf{f}_P^{n+1}(\mathbf{x}^{n+1}) &= \mathbf{m}^{n+1} - \eta_w^{n+1}(\boldsymbol{\theta}^{n+1}, \mathbf{P}^{n+1})\rho_w(\boldsymbol{\theta}^{n+1}) \\
&\quad - \eta_v^{n+1}(\boldsymbol{\theta}^{n+1}, \mathbf{P}^{n+1})\rho_v(\boldsymbol{\theta}^{n+1}, \mathbf{P}^{n+1}). \quad (76)
\end{aligned}$$

*Numerical algorithm.* The described numerical algorithm becomes:

*Step 1* Set  $T$ ,  $\Delta t$ ,  $N = T/\Delta t$

*Step 2* Set initial values  $P_0$ ,  $\theta_0$ ,  $\ell_0$ ,  $m_d(0) = 0$

*Step 3*

For  $n = 0, \dots, N - 1$

$t_n = n\Delta t$

update  $m_{d,eq}(\theta^n)$ ,  $F^n$

solve (62) to get  $\ell^{n+1}$

solve (61) to get  $m_d^{n+1}$

update  $P_\infty^{n+1}$ ,  $\theta_\infty^{n+1}$

update  $\mathbf{M}^n$ ,  $\mathbf{K}^n$ ,  $\mathbf{f}^{n+1}$

solve (65) by Newton's iteration procedure to get  $\mathbf{x}^{n+1}$

end  $n$

## 8. Material data for concrete at high temperatures

Based on the literature review, the material properties of concrete and its components subjected to high temperatures are assumed as follows.

The free thermal strain of concrete,  $\epsilon_\theta$  [-], is defined in the temperature range of 293.15 K to 1473.15 K as [2, Section 3.3.1]

for siliceous aggregates concrete:

$$\epsilon_\theta(\theta) = \begin{cases} -1.8 \times 10^{-4} + 9 \times 10^{-6} \theta + 2.3 \times 10^{-11} \theta^3 & \text{for } \theta \leq 973.15 \text{ K,} \\ 14 \times 10^{-3} & \text{for } \theta > 973.15 \text{ K,} \end{cases} \quad (77)$$

for calcareous aggregates concrete:

$$\epsilon_\theta(\theta) = \begin{cases} -1.2 \times 10^{-4} + 6 \times 10^{-6} \theta + 1.4 \times 10^{-11} \theta^3 & \text{for } \theta \leq 1078.15 \text{ K,} \\ 12 \times 10^{-3} & \text{for } \theta > 1078.15 \text{ K.} \end{cases} \quad (78)$$

The constitutive law for concrete in compression,  $\sigma = \mathcal{L}(\epsilon_m, \theta)$ , is adopted from Eurocode 2 in the form [2, Section 3.2.2.1]

$$\sigma(\epsilon_m, \theta) = \begin{cases} -\frac{3\epsilon_m f_c(\theta)}{\epsilon_{c1}(\theta) \left[ 2 + \left( \frac{\epsilon_m}{\epsilon_{c1}(\theta)} \right)^3 \right]} & \text{for } \epsilon_{cu1}(\theta) < \epsilon_m \leq 0, \\ 0 & \text{for } \epsilon_m \leq \epsilon_{cu1}(\theta), \end{cases} \quad (79)$$

where  $\epsilon_m$  is the total mechanical strain,  $f_c$  is the compressive strength of concrete,  $\epsilon_{c1}$  is the strain corresponding to  $f_c$ , and  $\epsilon_{cu1}$  is the ultimate strain, see Figure 4 and Figure 5.

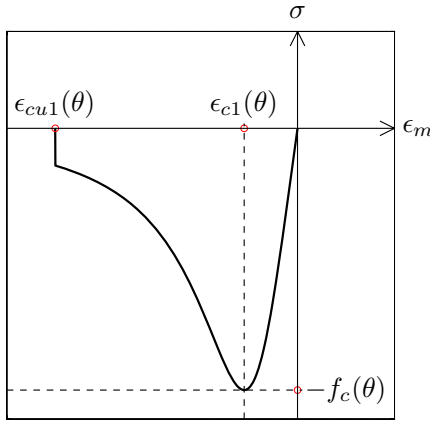


**Figure 4.** Constitutive law for concrete in compression given by Eurocode 2 [2, Figure 3.1]

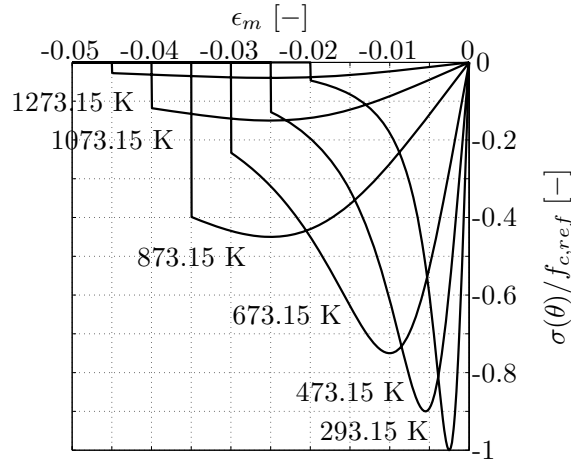


**Figure 5.** An example of the constitutive law for concrete in compression at high temperatures [2]

The temperature dependent parameters of the constitutive law (79),  $f_c(\theta)$ ,  $\epsilon_{c1}(\theta)$ , and  $\epsilon_{cu1}(\theta)$ , for the normal strength concrete with the siliceous and calcareous aggregates, NSC-S and NSC-C, respectively, as well as for three classes of high strength concrete (HSC-1, HSC-2, and HSC-3, see [2, Section 6.1]) are stated in Eurocode 2 in the form of tabulated data [2, Table 3.1, Table 6.1N] that are illustrated in Figures 6 and 7.

The constitutive law of concrete in tension need not be defined in our approach. It is sufficient to describe the tensile strength,  $f_t$  [Pa], that can be assumed as [17, eq. (34)]

$$f_t(\theta) = f_{t,ref} \times \begin{cases} 1 & \text{for } \theta \leq 373.15 \text{ K}, \\ (873.15 - \theta)/500 & \text{for } 373.15 \text{ K} < \theta \leq 823.15 \text{ K}, \\ (1473.15 - \theta)/6500 & \text{for } 823.15 \text{ K} < \theta \leq 1473.15 \text{ K}, \\ 0 & \text{for } \theta > 1473.15 \text{ K}, \end{cases} \quad (80)$$

where  $f_{t,ref}$  [Pa] is the reference tensile strength of concrete at the room temperature.

If the reference tensile strength,  $f_{t,ref}$  [Pa], is not known, it can be estimated from the reference compressive strength of concrete at the room temperature,  $f_{c,ref}$  [MPa].

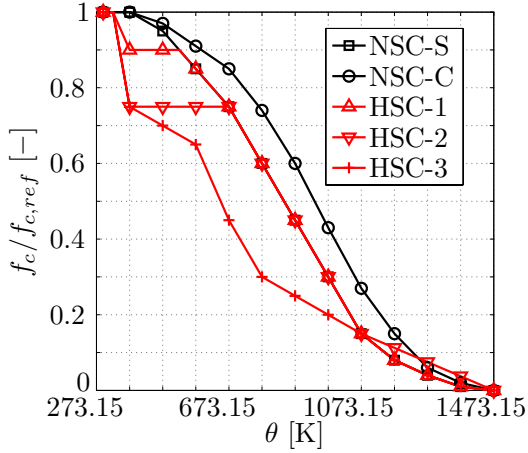


**Figure 6.** Reduction of the compressive strength of NSC and HSC given by Eurocode 2 [2]

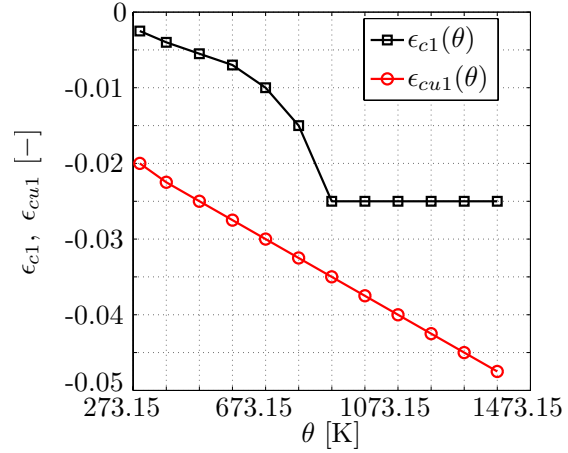


**Figure 7.** Temperature evolution of the mechanical strains of concrete according to Eurocode 2 [2]

In Eurocode 2 [1, Table 3.1], the tensile strength of high strength concrete is defined as

$$f_{t,ref} = 2.12 \ln \left( 1 + \frac{f_{c,ref}}{10} \right) \quad [\text{MPa}]. \quad (81)$$

The Young's modulus of concrete,  $E_c$  [Pa], can be easily derived from (79) in the form (see e.g. [18, eq. (3.14)])

$$E_c(\theta) = \frac{3f_c(\theta)}{2\epsilon_{c1}(\theta)}. \quad (82)$$

The Poisson's ratio of concrete,  $\nu$  [-], is usually taken as temperature independent (see e.g. [3, p. 46]) since the data about its temperature dependency are ambiguous [46, Section 2.2.1.2]. Here, we follow the assumption (which leads to conservative results) that the Poisson's ratio increases with increasing temperature. Based on the data experimentally determined by [42, pp. 132–133] for high strength concrete ( $f_{c,ref} \approx 60$  MPa), we assume that

$$\nu(\theta) = \begin{cases} 0.2 & \text{for } \theta \leq 293.15 \text{ K,} \\ 0.2 + 0.5(\theta - 293.15)/580 & \text{for } 293.15 \text{ K} < \theta \leq 873.15 \text{ K,} \\ 0.7 & \text{for } \theta > 873.15 \text{ K.} \end{cases} \quad (83)$$

The eccentricity,  $e_F$  [-], used in the failure function of concrete (Section ??) generally depends on the type of concrete and probably also on temperature. Here, we assume constant (temperature independent) value,  $e_F = 0.505$ , derived from the data measured by [29, Table 2] for high strength concrete ( $f_{c,ref} \approx 60$  MPa) under biaxial compression tests at high temperatures, see Figure 8, where  $f_c(\theta)$  is taken from [29, Table 2],  $f_t(\theta)$  is assumed according to (80), with  $f_{t,ref} = 4$  MPa, and  $F(\theta)$  is determined by (26), with  $\sigma_3 = 0$ .

The porosity of concrete,  $\phi$  [-], may be expressed as [21, eq. (41)]

$$\phi(\theta) = \phi_{ref} + A_\phi(\theta - \theta_{ref}), \quad (84)$$

where  $\phi_{ref}$  [-] is the reference porosity (at the reference temperature,  $\theta_{ref}$  [K]), and  $A_\phi$  [K<sup>-1</sup>] is a concrete-type-depend constant (see [21, pp. 46–47]).

The thermal conductivity of concrete,  $\lambda_c$  [W m<sup>-1</sup> K<sup>-1</sup>], is given by [21, eqs. (46–47)]

$$\lambda_c(P, \theta) = \lambda_d(\theta) \left( 1 + \frac{4\phi(\theta)\rho_w(\theta)S_w(P, \theta)}{(1 - \phi(\theta))\rho_s} \right), \quad (85)$$

with

$$\lambda_d(\theta) = \lambda_{d,ref} [1 + A_\lambda(\theta - \theta_{ref})], \quad (86)$$

where  $\lambda_{d,ref}$  [W m<sup>-1</sup> K<sup>-1</sup>] is the reference thermal conductivity of a dry concrete (at the reference temperature,  $\theta_{ref}$  [K]), and  $A_\lambda$  [K<sup>-1</sup>] is an experimentally determined coefficient.

For the intrinsic permeability of concrete,  $K$  [m<sup>2</sup>], we adopt the Bary function recommended by [16, eq. (13)]

$$K(P, \theta) = K_{ref} \times 10^{4D(P, \theta)}, \quad (87)$$

where  $K_{ref}$  [m<sup>2</sup>] is the reference permeability at the room temperature, and  $D$  [-] is the multiplicative damage parameter that can be defined as [15, eq. (70)], [24, eq. (54)]

$$D(P, \theta) = D_m(P, \theta) + D_\theta(\theta) - D_m(P, \theta)D_\theta(\theta), \quad (88)$$

where  $D_m$  [-] is the mechanical damage parameter, which is assumed to be equal to the failure parameter (31) in our approach, i.e.

$$D_m(P, \theta) = F(P, \theta), \quad (89)$$

and  $D_\theta$  [-] is the thermal damage parameter that we define as (cf. [24, eq. (52)])

$$\begin{aligned} D_\theta(\theta) &= 1 - \frac{1}{3} (D_{\theta, Ec} + D_{\theta, fc} + D_{\theta, ft}) \\ &= 1 - \frac{1}{3} \left( \frac{E_c(\theta)}{E_{c,ref}} + \frac{f_c(\theta)}{f_{c,ref}} + \frac{f_t(\theta)}{f_{t,ref}} \right). \end{aligned} \quad (90)$$

It should be noted that usually, the thermal damage parameter is based only on the degradation of the Young's modulus (see [15, eqs. (29–30)], [24, eq. (52)]). This is however not possible to assume in our approach since we employ the constitutive model proposed by Eurocode 2 [2], see (79), where the stress is expressed as a function of the total mechanical strain,  $\epsilon_m$ , instead of the instantaneous stress-related strain,  $\epsilon_\sigma$ , and hence the resulting softening of the material with increasing temperature is higher than in reality (see also [4, 28]). In order to eliminate this effect, we propose to include not only the temperature dependent degradation of  $E_c$  but also the reduction of the other mechanical properties ( $f_c$ ,  $f_t$ ), which leads to good agreement of the resulting thermal damage parameter with the data stated in literature, see Figure 9.

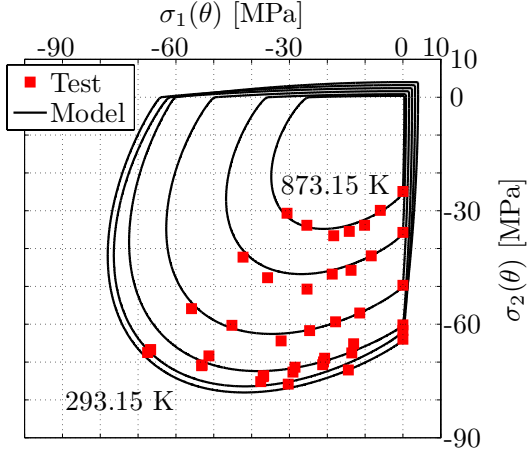


**Figure 8.** Comparison of failure function (26) used in our model with the experimental data measured by [29, Table 2]

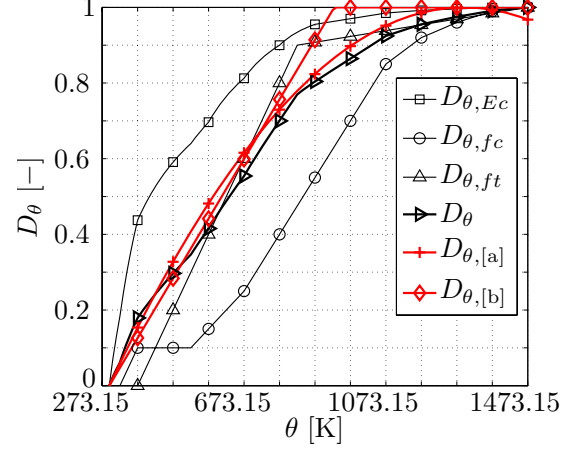


**Figure 9.** Thermal damage assumed in our model ( $D_\theta$ ) and its comparison with [15, eq. (30)] ( $D_{\theta,[a]}$ ) and [24, eq. (52)] ( $D_{\theta,[b]}$ )

The gas relative permeability and the liquid water relative permeability,  $K_{rg}$  [-] and  $K_{rw}$  [-], respectively, can be expressed by the formulas experimentally determined by [12, eqs. (7–9)]

$$K_{rg}(P, \theta) = 10^{S_w(P, \theta) \psi(\theta)} - 10^{\psi(\theta)} S_w(P, \theta), \quad (91)$$

$$K_{rw}(P, \theta) = 10^{(1-S_w(P, \theta)) \psi(\theta)} - 10^{\psi(\theta)} (1 - S_w(P, \theta)), \quad (92)$$

with

$$\psi(\theta) = 0.05 - 22.5 \phi(\theta). \quad (93)$$

The gas dynamic viscosity,  $\mu_g$  [Pa s], is approximated as [21, eq. (50)]

$$\mu_g(P, \theta) = \mu_{gv}(\theta) + [\mu_{ga}(\theta) - \mu_{gv}(\theta)] \left( \frac{P_a}{P + P_a} \right)^{0.608}, \quad (94)$$

with

$$\mu_{gv}(\theta) = \mu_{gv,ref} + \alpha_v(\theta - \theta_{ref}) \quad (95)$$

and

$$\mu_{ga}(\theta) = \mu_{ga,ref} + \alpha_a(\theta - \theta_{ref}) + \beta_a(\theta - \theta_{ref})^2, \quad (96)$$

where  $\mu_{gv,ref} = 8.85 \times 10^{-6}$  Pa s,  $\alpha_v = 3.53 \times 10^{-8}$  Pa s K<sup>-1</sup>,  $\mu_{ga,ref} = 17.17 \times 10^{-6}$  Pa s,  $\alpha_a = 4.73 \times 10^{-8}$  Pa s K<sup>-1</sup>,  $\beta_a = 2.22 \times 10^{-11}$  Pa s K<sup>-2</sup>, and  $\theta_{ref} = 273.15$  K.

The liquid water dynamic viscosity,  $\mu_w$  [Pa s], can be calculated from [21, eq. (51)]

$$\mu_w(\theta) = 0.6612(\theta - 229)^{-1.532}. \quad (97)$$

The volume fraction of liquid (all free) water,  $\eta_w$  [-], is governed by the sorption isotherm function proposed by Bažant *et al.* [6, 7, 8]. After some modification related to the saturated region ( $P/P_s \geq 1.0$ ), see [15, eq. (73)], we can write

$$\text{if } \theta \leq \theta_{cr} : \quad \eta_w(P, \theta) = \begin{cases} \frac{c}{\rho_w(\theta)} \left( \frac{\phi(\theta_{ref})\rho_w(\theta_{ref})}{c} \frac{P}{P_s(\theta)} \right)^{1/m(\theta)} & \text{for } \frac{P}{P_s(\theta)} \leq 0.96, \\ \sum_{i=0}^3 \xi_i(\theta) \left( \frac{P}{P_s(\theta)} - 0.96 \right)^i & \text{for } 0.96 < \frac{P}{P_s(\theta)} < 1.00, \\ \phi(\theta) & \text{for } \frac{P}{P_s(\theta)} \geq 1.00, \end{cases} \quad (98)$$

$$\text{if } \theta > \theta_{cr} : \\ \eta_w = 0,$$

with

$$m(\theta) = 1.04 - \frac{(\theta - 263.15)^2}{22.34(\theta_{ref} - 263.15)^2 + (\theta - 263.15)^2}, \quad (99)$$

where  $c$  [ $\text{kg m}^{-3}$ ] is the mass of cement per unit volume of concrete,  $\theta_{ref}$  [K] is the reference temperature ( $\theta_{ref} = 298.15$  K), the term  $[\phi(\theta_{ref})\rho_w(\theta_{ref})]$  expresses the saturation water content at 298.15 K, and  $\xi_i(\theta)$  are temperature dependent coefficients that ensure a smooth transition between the unsaturated and saturated region, thus the sorption isotherm function and its first derivative with respect to ( $P/P_s(\theta)$ ) are continuous (cf. [14, 15, 40, 52]). Therefore, we can write

$$\xi_0(\theta) = \eta_{w,0.96}(\theta), \quad (100)$$

$$\xi_1(\theta) = \eta'_{w,0.96}(\theta), \quad (101)$$

$$\xi_2(\theta) = \frac{3(\eta_{w,1.00}(\theta) - \eta_{w,0.96}(\theta))}{0.04^2} - \frac{2\eta'_{w,0.96}(\theta) + \eta'_{w,1.00}(\theta)}{0.04}, \quad (102)$$

$$\xi_3(\theta) = \frac{2(\eta_{w,0.96}(\theta) - \eta_{w,1.00}(\theta))}{0.04^3} + \frac{\eta'_{w,0.96}(\theta) + \eta'_{w,1.00}(\theta)}{0.04^2}, \quad (103)$$

where

$$\eta_{w,0.96}(\theta) = \frac{c}{\rho_w(\theta)} \left( \frac{\phi(\theta_{ref})\rho_w(\theta_{ref})}{c} 0.96 \right)^{1/m(\theta)}, \quad (104)$$

$$\eta_{w,1.00}(\theta) = \phi(\theta),$$

and

$$\eta'_{w,0.96}(\theta) = \frac{d\eta_{w,0.96}(\theta)}{d\theta} \quad \text{and} \quad \eta'_{w,1.00}(\theta) = \frac{d\eta_{w,1.00}(\theta)}{d\theta}. \quad (105)$$

The degree of saturation with liquid water,  $S_w$  [-], is defined as

$$S_w(P, \theta) = \frac{\eta_w(P, \theta)}{\phi(\theta)}. \quad (106)$$

The mass of dehydrated water,  $m_d$  [ $\text{kg m}^{-3}$ ], is governed by equation (12), with [19, eq. (8)], [13, eq. (C-22)], [3, eq. (1.9)]

$$m_{d,eq}(\theta) = \frac{7.5}{100} m_{eq}^{378.15} \left[ 1 - \exp\left(-\frac{\theta - 378.15}{200}\right) \right] H(\theta - 378.15)$$

$$\begin{aligned}
& + \frac{2}{100} m_{eq}^{378.15} \left[ 1 - \exp \left( -\frac{\theta - 673.15}{10} \right) \right] H(\theta - 673.15) \quad (107) \\
& + \frac{1.5}{100} m_{eq}^{378.15} \left[ 1 - \exp \left( -\frac{\theta - 813.15}{5} \right) \right] H(\theta - 813.15),
\end{aligned}$$

where  $m_{eq}^{378.15}$  [kg m<sup>-3</sup>] is the equilibrium mass at 378.15 K and  $H$  is the Heaviside function.

In [13, p. 146], the following values of material parameters that belong to equations (12) and (107) are stated:  $\tau = 10800$  s,  $m_{eq}^{378.15} = 210$  kg m<sup>-3</sup>, which are also adopted in our simulations, since these parameters are usually not measured within the fire tests.

The density of solid skeleton,  $\rho_s$  [kg m<sup>-3</sup>], is, together with the concrete porosity and the mass of water released into the pores by dehydration, governed by the solid mass conservation equation (??), cf. [21, pp. 47–48]. In our approach, the density of solid skeleton is assumed to be a constant value. As obvious from numerical experiments, this simplification has negligible effect on the obtained results.

The density of liquid water,  $\rho_w$  [kg m<sup>-3</sup>], can be expressed by the experimentally determined formula, originally proposed by [20, eq. (4.79)] and simplified by [23, eq. (35)] (neglecting the water pressure dependence of  $\rho_w$ ), of the form

$$\rho_w(\theta) = \sum_{i=0}^5 a_i (\theta - 273.15)^i (-1 \times 10^7) + \sum_{i=0}^5 b_i (\theta - 273.15)^i \quad \text{for } \theta \leq \theta_{cr}, \quad (108)$$

where  $a_0 = 4.8863 \times 10^{-7}$ ,  $a_1 = -1.6528 \times 10^{-9}$ ,  $a_2 = 1.8621 \times 10^{-12}$ ,  $a_3 = 2.4266 \times 10^{-13}$ ,  $a_4 = -1.5996 \times 10^{-15}$ ,  $a_5 = 3.3703 \times 10^{-18}$ ,  $b_0 = 1.0213 \times 10^3$ ,  $b_1 = -7.7377 \times 10^{-1}$ ,  $b_2 = 8.7696 \times 10^{-3}$ ,  $b_3 = -9.2118 \times 10^{-5}$ ,  $b_4 = 3.3534 \times 10^{-7}$ ,  $b_5 = -4.4034 \times 10^{-10}$ .

The specific enthalpy of evaporation,  $h_e$  [J kg<sup>-1</sup>], can be expressed by the Watson formula [21, eq. (49)], [26, eq. (28)], [14, eq. (AI.27)]

$$h_e(\theta) = \begin{cases} 2.672 \times 10^5 (\theta_{cr} - \theta)^{0.38} & \text{for } \theta \leq \theta_{cr}, \\ 0 & \text{for } \theta > \theta_{cr}. \end{cases} \quad (109)$$

The specific enthalpy of dehydration,  $h_d$  [J kg<sup>-1</sup>], is considered to be a constant value [14, eq. (AI.26)]

$$h_d = 2400 \times 10^3 \text{ J kg}^{-1}. \quad (110)$$

The specific heat capacity of liquid water,  $c_p^w$  [J kg<sup>-1</sup> K<sup>-1</sup>], is given by [14, eq. (AI.29)]

$$c_p^w(\theta) = (2.4768 \theta + 3368.2) + \left( \frac{a \theta}{513.15} \right)^b \quad \text{for } \theta \leq \theta_{cr}, \quad (111)$$

where  $a = 1.08542631988638$  and  $b = 31.4447657616636$ .

The specific heat capacity of solid skeleton,  $c_p^s$  [J kg<sup>-1</sup> K<sup>-1</sup>], can be calculated from [14, eq. (AI.30)]

$$c_p^s(\theta) = 900 + 80 \frac{\theta - 273.15}{120} - 4 \left( \frac{\theta - 273.15}{120} \right)^2. \quad (112)$$

For the specific heat capacity of water vapour,  $c_p^v$  [ $\text{J kg}^{-1} \text{K}^{-1}$ ], the following equation is proposed by [14, eq. (AI.31)]

$$c_p^v(\theta) = \begin{cases} (7.1399\theta - 443) + \left(\frac{a\theta}{513.15}\right)^b & \text{for } \theta \leq \theta_{cr}, \\ 45821.01 & \text{for } \theta > \theta_{cr}, \end{cases} \quad (113)$$

where  $a = 1.13771502228162$  and  $b = 29.4435287521143$ .

It should be noted that above the critical temperature (if  $\theta > \theta_{cr}$ ), there is no liquid water in concrete (see equation (98)) and hence, the liquid water properties ( $\rho_w$ ,  $c_p^w$ ), need not be defined.

## 9. Numerical results and experiments

In order to validate the model presented in this paper, the results obtained by numerical simulations are compared with the experimentally determined data. Three experiments reported in literature are closely investigated:

- the test of the hygro-thermal behaviour of high strength concrete ( $f_{c,ref} \approx 90$  MPa) prismatic specimen  $300 \times 300 \times 120$  mm<sup>3</sup> under unidirectional heating by the radiant heater of a temperature of 600 °C reported by Kalifa *et al.* in [35] and related publications [34, 36];
- the test of the hygro-thermal behaviour of high strength concrete ( $f_{c,ref} \approx 60$  MPa) prismatic specimen  $300 \times 300 \times 120$  mm<sup>3</sup> under unidirectional heating by the radiant heater of a temperature of 600 °C reported by Mindeguia in [42] and related publication [44];
- the test of the spalling behaviour of high strength concrete ( $f_{c,ref} \approx 60$  MPa) prismatic specimen  $700 \times 600 \times 150$  mm<sup>3</sup> under unidirectional heating by the ISO 834 fire reported by Mindeguia in [42] and related publication [43].

Within the first two of the above tests, the pore pressure and the temperature propagation through the specimen as well as its mass loss were recorded. This type of tests is therefore denoted as the "PTM test" by Mindeguia [42], which is also adopted in this paper. It should be noted that no spalling was observed during the both PTM experiments and hence, these tests are employed primarily for the validation of the hygro-thermal behaviour simulation while the spalling prediction can be validated only on the qualitative level (whether it occurs or not). For that reason, the third test is also analysed, since it enables to validate our model also with respect to the quantitative prediction of spalling (i.e. the prediction of the amount of the potential spalling).

### 9.1. Simulation of the PTM test 1

The Kalifa's experiments [34, 35, 36] have been accepted as a benchmark problem by many authors focused on modelling of concrete subjected to high temperatures (cf. [3,

Section III-3]; [15, Section 3.2]; [17, Section 5]; [22, Section 6.1]; [23, Section 6.2]; [38, Sections 4.3, 5.4]; [47, Section 6.4]; [54, Section 3.1]).

In [36], we can find the high temperature thermal and hygral properties measured by Kalifa *et al.* for 4 types of concrete named as M30, M75C, M75SC and M100C. The M30 and M100 concretes were used for the subsequent PTM tests reported by Kalifa *et al.* in [35]. Within this experiment, the specimens were subjected to an unidirectional heating up to 450 °C, 600 °C, and 800 °C using a radiant heater. Moreover, similar experiment – in this case for the specimens made of C110 concrete (practically the same as the M100 concrete, only with a little bit higher amount of cement and superplasticizer, see [34]) with polypropylene fibres of the content of (0–3) kg m<sup>-3</sup>, were made by Kalifa *et al.* [34] in order to assess the effect of fibres on the high-temperature behaviour of high strength concrete.

For the validation of our model, the results measured by Kalifa *et al.* [35] for the M100 concrete heated up to 600 °C are employed. This case is chosen for the following reasons: our model is primarily designed to study the behaviour of high strength concrete (such as M100); material properties of the M100 concrete are described in detail in [36] (more comprehensive description than for the C110 concrete in [34]); and the results obtained for the other heating conditions (up to 450 °C or 800 °C) are not sufficiently reported in [35].

*9.1.1. Experiment description* The tests performed by Kalifa *et al.* are described in detail in [35]. Therefore, only a brief description of the experiment is stated below.

As mentioned above, two types of concrete (M30 and M100) and three different heating conditions (450 °C, 600 °C, and 800 °C) were used by Kalifa *et al.* [35]. Hereafter, only the case of M100 – 600 °C is assumed. Material (thermal and hygral) properties of the M100 concrete have been reported in study [36] and are discussed in Section 9.1.2.

As shown in Figure 10, the 300 × 300 120 mm<sup>3</sup> test specimen was subjected to an unidirectional heating (in the 120-mm direction) by a radiant heater of the temperature of 600 °C placed near its surface for a heating period of 6 hours.

Within the test, the temperature, the pore pressure, and the mass loss of the specimen were recorded. The temperature together with the pore pressure were measured using the combined pressure-temperature gauges (see [34, Figure 3]) placed at the distance of (10, 20, 30, 40, and 50) mm from the heated surface. The heated surface temperature was measured by a thermocouple placed at the depth of 2 mm. Moreover, as obvious from the graphs listed in [35], the temperature on the unexposed side was also recorded (probably by an additional thermocouple or by a surface thermometer). The mass loss was monitored by a balance on which the specimen was placed during the test (see Figure 10).

*9.1.2. Modelling* In this section, the material properties of concrete, the initial and boundary conditions as well as the discretization employed for the numerical modelling are discussed. The thermal and hygral properties of concrete are assumed according

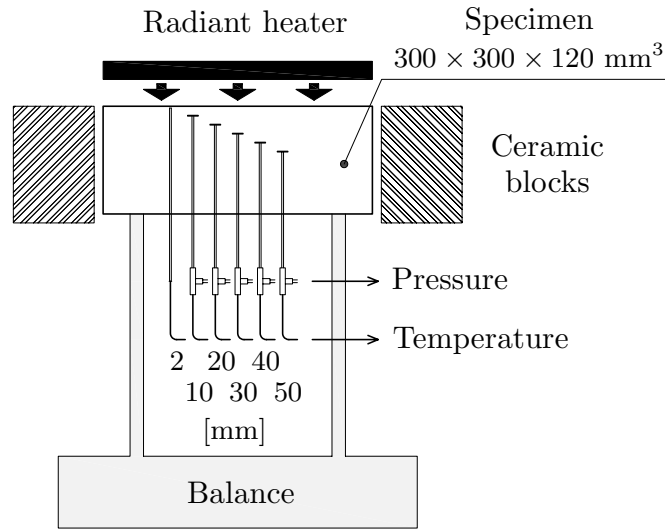


**Figure 10.** Scheme of the test set-up (according to Kalifa *et al.* [35, Figure 2])

to the relationships given in Section 8, with the parameters determined from the data measured by Kalifa *et al.* [36]. All the parameters are summarized in Table 1.

**Table 1.** Material properties and parameters used in our simulation of the PTM test 1 by Kalifa *et al.* [35]

Parameter	Value	Unit	Reference
Type of concrete	HSC2-C	–	[2, 36]
$f_{c,ref}$	91.8	MPa	[36, Table 1]
$f_{t,ref}$	4.9	MPa	[1], see (81)
$c$	414.8	$\text{kg m}^{-3}$	[36, Table 1]
$\theta_{ref}$	293.15	K	determined from
$\phi_{ref}$	0.0897	–	[36, Table 2],
$A_\phi$	$2.4457 \times 10^{-5}$	$\text{K}^{-1}$	see Figure 11
$\rho_s$	2660	$\text{kg m}^{-3}$	determined from
			[36, Table 4],
			see Figure 13
$\theta_{ref}$	293.15	K	determined from
$\lambda_{d,ref}$	1.9759	$\text{W m}^{-1} \text{K}^{-1}$	[36, Table 7],
$A_\lambda$	$-6.4215 \times 10^{-4}$	$\text{K}^{-1}$	see Figure 14
$K_{ref}$	$1.3 \times 10^{-20}$	$\text{m}^2$	–

The concrete of the test specimens (named as M100 concrete in [35, 36]) is assumed to be a high strength concrete, class 2 (see [2, Section 6.1] and Section 8), with calcareous aggregates, which can be denoted as "HSC2-C". This classification determines the free

thermal strain of concrete and the temperature dependent reduction of its compressive strength according to Eurocode 2 [2], as described in Section 8.

The reference compressive strength of concrete at the room temperature is taken from [36, Table 1]. The reference tensile strength of concrete at the room temperature is not specified in [35, 36] and hence, it is calculated by (81).

The mass of cement per unit volume of concrete is taken from [36, Table 1].

For the porosity of concrete, the parameters of equation (84) are determined by a linear regression of the data stated in [36, Table 2], see Figure 11.

Assuming the above values of  $c$  and  $\phi(\theta)$ , the resulting degree of saturation with liquid water (106), based on the sorption isotherms (98), is illustrated in Figure 12.

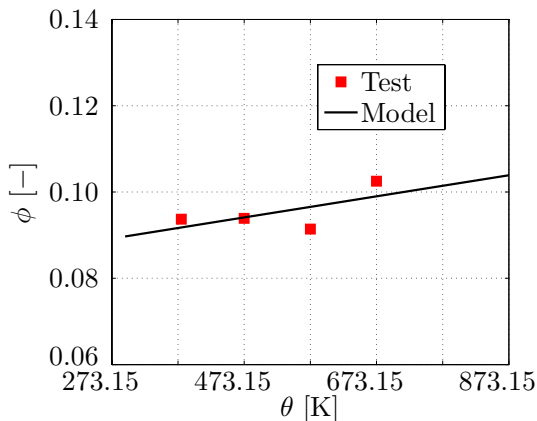


**Figure 11.** Porosity of concrete measured by [36] (points) and assumed in our model (line)

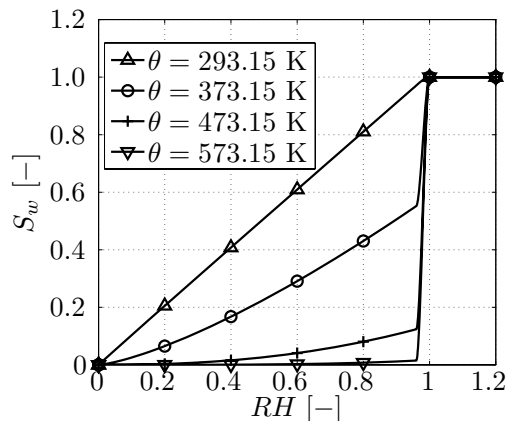


**Figure 12.** Degree of saturation with liquid water assumed in our model

As mentioned in Section 8, the density of solid skeleton,  $\rho_s$ , is assumed to be a constant value in our approach. This value can be estimated from the data measured by Kalifa *et al.* [36, Table 4] for the apparent density. The corresponding apparent density assumed in our model, that can be expressed as (cf. [24, eq. (26)])

$$\begin{aligned} \rho &= \rho_w \eta_w + \rho_g \eta_g + \rho_s \eta_s \\ &= \rho_w (\phi S_w) + (\rho_v + \rho_a) [\phi (1 - S_w)] + \rho_s (1 - \phi), \end{aligned} \quad (114)$$

appears in Figure 13.

The temperature dependence of the thermal conductivity of concrete was measured by Kalifa *et al.* [36, Table 7] at a dry state. The parameters of equation (86) are determined by a linear regression of the measured data, see Figure 14 ( $RH = 0$ ). The resulting thermal conductivity of concrete assumed in our model is shown in Figure 14.

The intrinsic permeability of concrete was tested by Kalifa *et al.* [36, Table 6] on concrete samples dried at 105 °C and then heated up to several temperature levels. However, the reference permeability of undamaged concrete at the room temperature

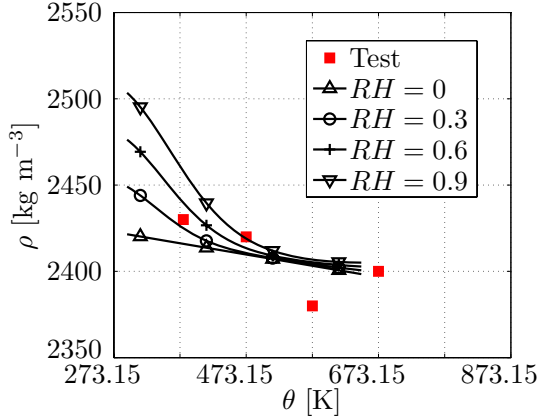


**Figure 13.** Apparent density of concrete measured by [36] at a dry state (points) and assumed in our model (lines)

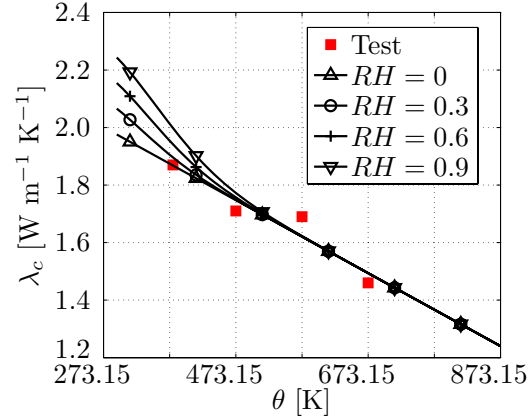


**Figure 14.** Thermal conductivity of concrete measured by [36] at a dry state (points) and assumed in our model (lines)

is not reported in [36] and hence it is determined by a trial-and-error method in our simulation (cf. [54, p. 277]).

Scheme of the analyzed problem is displayed in Figure 15. The spatial discretization is performed with the use of linear 1-D elements. In total, 120 elements are employed – 30 elements in the interval  $x \in (0, \ell/2)$ , 30 elements for  $x \in (\ell/2, 3\ell/4)$  and 60 elements in the interval  $x \in (3\ell/4, \ell)$ . For the time discretization, the time step is set to  $\Delta t = 1$  s. The characteristic time of spalling is assumed as  $\gamma = 10$  s.

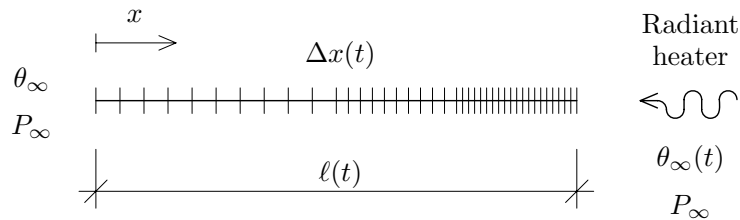


**Figure 15.** Scheme of the analyzed problem

The initial conditions are assumed as  $P_0 = 1.9039 \times 10^3$  Pa,  $\theta_0 = 293.15$  K,  $\ell_0 = 0.12$  m. For these values, the initial saturation with liquid water  $S_{w,0} = 0.77$ , which is the value reported by Kalifa *et al.* [35, Table 2].

As stated above, a radiant heater of a temperature of 600 °C was employed for the experiment. However, as mentioned by e.g. Gawin *et al.* [23, pp. 554–556], the temperature of the ambient air on the heated side, which needs to be defined for the boundary conditions assumed in the model (see Section 4), is lower than the temperature of the heater. For our simulation, the ambient temperature on the heated side,  $\theta_\infty$  [K],

has been determined by a trial-and-error method as (see Figure 16)

$$\theta_{\infty}(t) = \begin{cases} 293.15 + t \frac{410}{300} & \text{for } t \leq 300 \text{ s,} \\ 703.15 + (t - 300) \frac{35}{21300} & \text{for } t > 300 \text{ s,} \end{cases} \quad (115)$$

where  $t$  [s] is the time of heating.

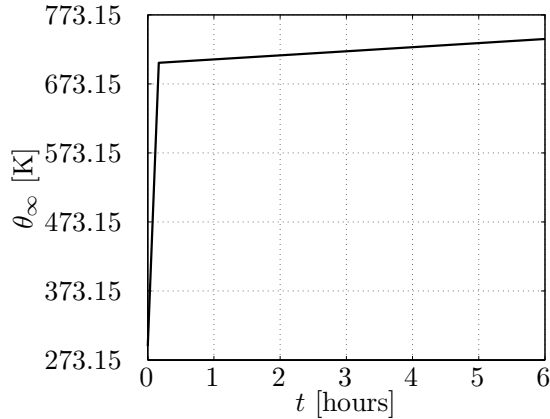


**Figure 16.** Air temperature on the heated side of the specimen used for the simulation of the PTM test 1

The boundary conditions are summarized in Table 2.

**Table 2.** Boundary conditions parameters for simulation of PTM test 1

Variable	Value		Unit
	Unexposed side	Exposed side	
$P_{\infty}$	$P_0$	$P_0$	Pa
$\theta_{\infty}$	$\theta_0$	$\theta_{\infty}(t)$ , see (115)	K
$\alpha_c$	4	20	$\text{W m}^{-2} \text{K}^{-1}$
$e\sigma_{SB}$	$0.7 \times 5.67 \times 10^{-8}$	$0.7 \times 5.67 \times 10^{-8}$	$\text{W m}^{-2} \text{K}^{-4}$
$\beta_c$	0.009	0.019	$\text{m s}^{-1}$

*9.1.3. Discussion* The resulting pore pressure, temperature and mass loss evolutions determined by our simulation are compared with the experimentally measured data in Figures 17–19 (note that the distances in millimeters stated in the figures are, in accordance with [35], measured from the heated surface).

The pore pressure evolution in the depth of 30 mm from the heated surface is not displayed in Figure 17 since it was not correctly measured by Kalifa *et al.* [35], probably

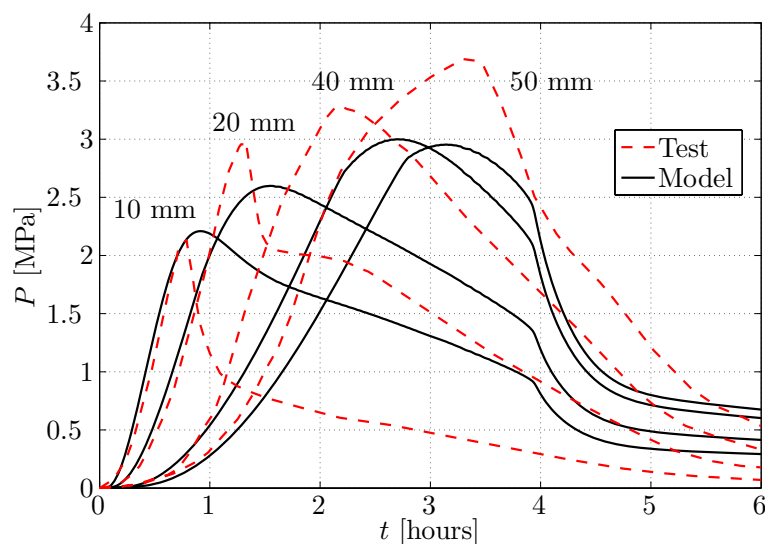


**Figure 17.** Pore pressure evolution measured by [35, Figure 4] (dashed lines) and determined by the present model (solid lines)

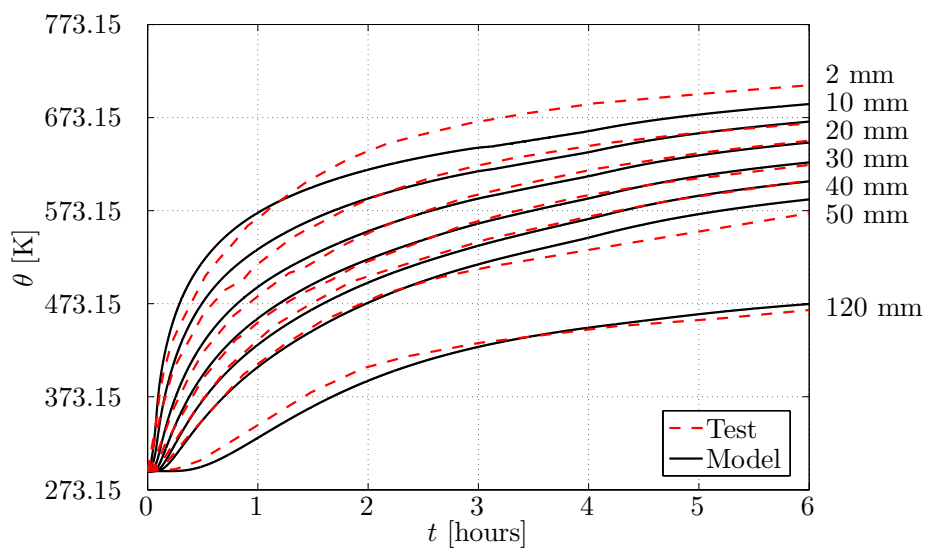


**Figure 18.** Temperature evolution measured by [35, Figure 4] (dashed lines) and determined by the present model (solid lines)

due to the damage of the gauge, see Kalifa *et al.* [35, p. 1923]. On the other hand, the pore pressure evolution in the depths of (10, 20, and 50) mm can be verified more precisely because the investigated PTM test was duplicated and the data from the both measurements are stated in [35, Figure 6], see Figures 20–22.

From Figures 17–22, it is obvious that in this case, the present model predicts the hygro-thermal behaviour of the heated concrete specimen on the sufficient level of

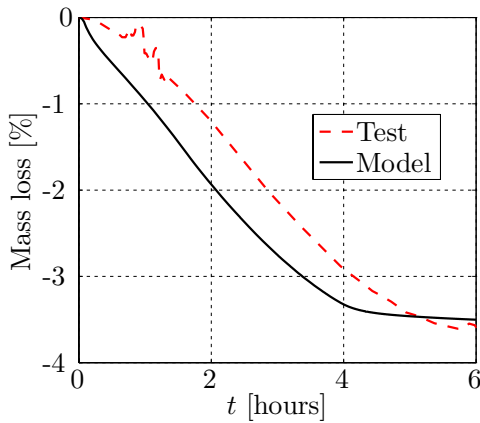


**Figure 19.** Mass loss measured by [35, Figure 7]) (dashed line) and determined by the present model (solid line)

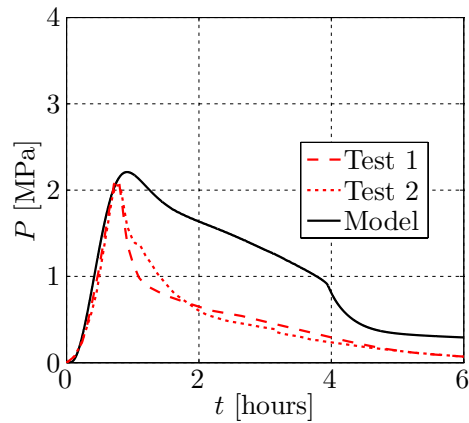


**Figure 20.** Pore pressure development measured by [35, Figure 6] and determined by the present model at the depth of 10 mm from the heated surface

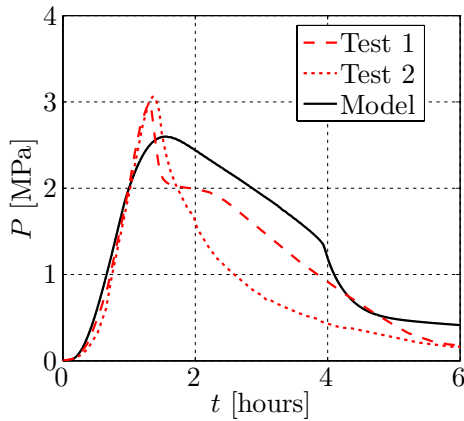


**Figure 21.** Pore pressure development measured by [35, Figure 6] and determined by the present model at the depth of 20 mm from the heated surface

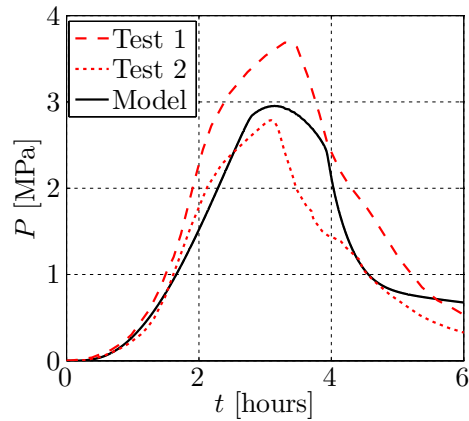


**Figure 22.** Pore pressure development measured by [35, Figure 6] and determined by the present model at the depth of 50 mm from the heated surface

accuracy. The spalling behaviour is also simulated correctly since, as mentioned above, during the test, no spalling was observed by Kalifa *et al.* [35], which is in accordance with our simulation, see Figure 23 – the maximal value of failure function (31) achieved within the specimen during the test period does not exceeds the value of 1. The evolution of the maximal values of the damage parameter and its components within the specimen during the test period determined by our model is shown in Figure 24.

For illustration, the spatial and time distributions of the primary unknowns of the present model (except the thickness of the specimen, which is constant in this case) for

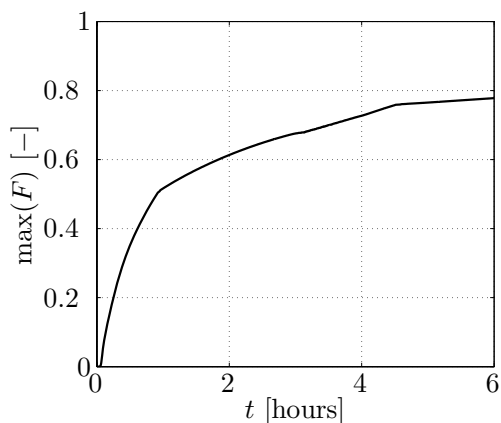


**Figure 23.** Evolution of the failure parameter

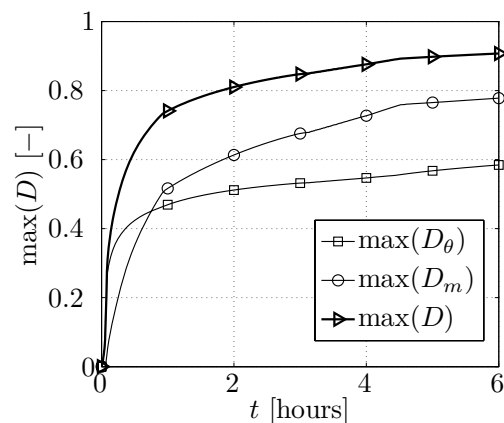


**Figure 24.** Evolution of the damage parameter

the Kalifa's PTM test 1 [35] are shown in Figures 25 and 26.

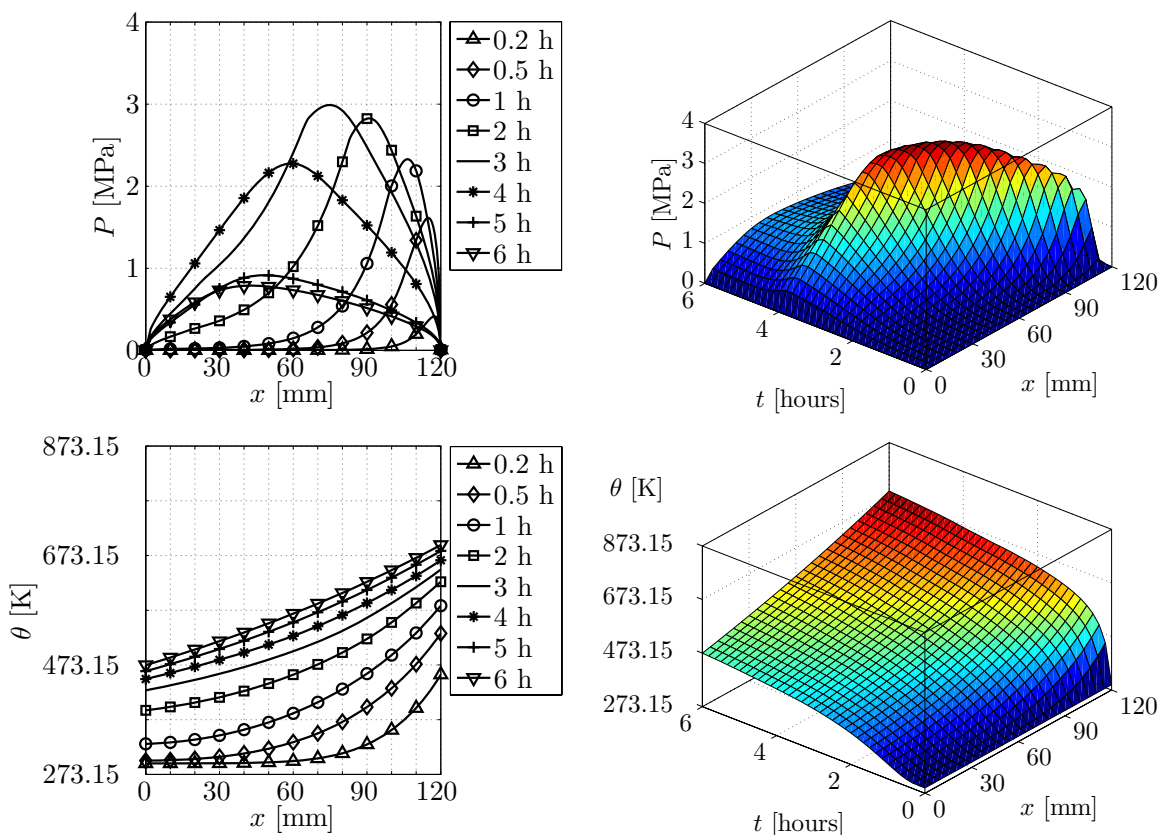


**Figure 25.** Distribution of  $P$  and  $\theta$  for the analyzed PTM test 1 [35]

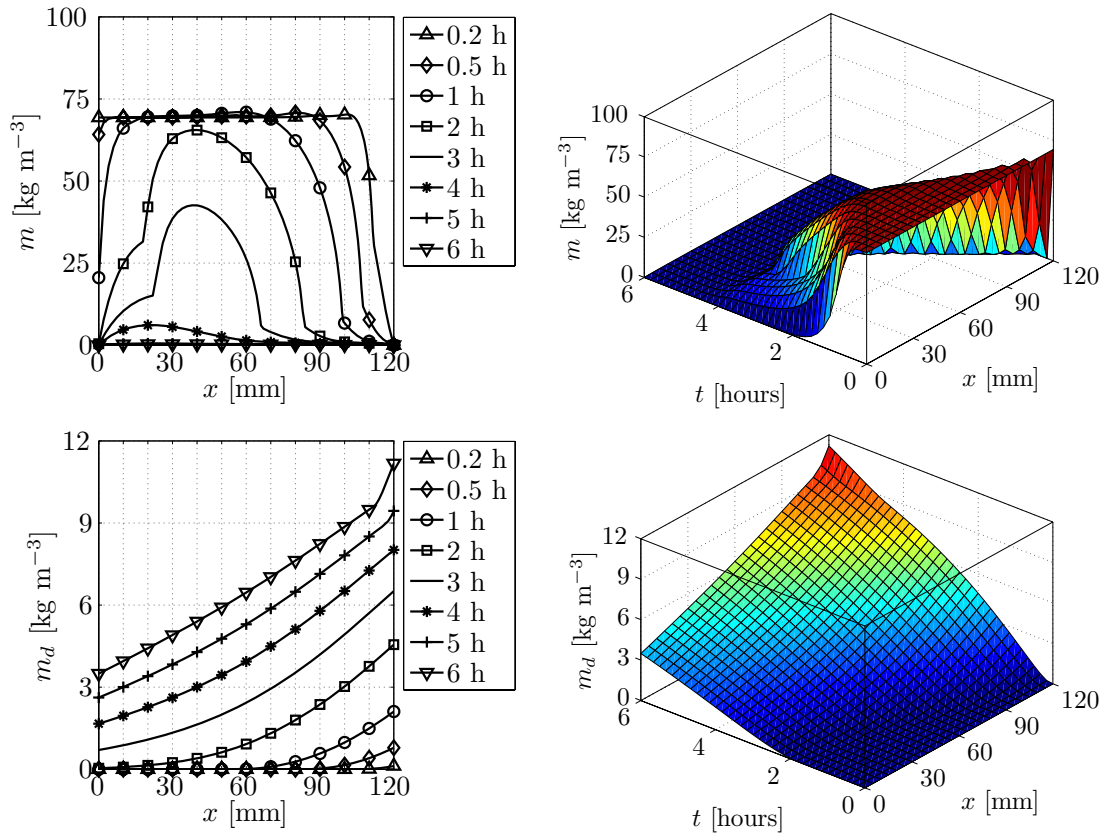


**Figure 26.** Distribution of  $m$  and  $m_d$  for the analyzed PTM test 1 [35]

## 9.2. Simulation of the PTM test 2

**9.2.1. Experiment description** The PTM test procedure proposed by Kalifa *et al.* [35] was adopted by Mindeguia as a part of an extended experimental program reported in [42] and [43, 44]. Within this program, the material properties investigation, hygro-thermal behaviour measurements (the PTM tests) and the spalling experiments were performed (a detailed summary of the experiments included in the program appears in [42, Section 1]). Hereafter, one of the PTM tests performed by [42] is closely investigated – the PTM test of a high strength concrete (denoted as "B60" in [42]) prismatic specimens (conditioned in "Air\_1" according to [42]) heated by a radiant heater of the temperature of 600 °C (the type of heating denoted as "modéré" in [42]) placed near its surface for a heating period of 5 hours. The test set-up is the same as described for the Kalifa's experiment (Section 9.1.1). Note that (i) within the investigated PTM test 2, no spalling was observed by Mindeguia [42], and (ii) the test was duplicated and the data from the both measurements of  $P$  are stated in [42], see Section 9.2.3.

**9.2.2. Modelling** The thermal and hygral properties of concrete are assumed according to the relationships given in Section 8, with the parameters determined from the data measured by Mindeguia [42]. All the parameters are summarized in Table 3.

**Table 3.** Material properties and parameters used in our simulation of the PTM test by Mindeguia [42]

Parameter	Value	Unit	Reference
Type of concrete	HSC1-C	–	[2, 42]
$f_{c,ref}$	61.0	MPa	[42, Table 24]
$f_{t,ref}$	3.76	MPa	
$c$	550	kg m <sup>-3</sup>	[42, Table 14]
$\theta_{ref}$	293.15	K	determined from
$\phi_{ref}$	0.1027	–	[42, Table 25],
$A_\phi$	$1.0624 \times 10^{-4}$	K <sup>-1</sup>	see Figure 27
$\rho_s$	2660	kg m <sup>-3</sup>	determined from [42, Table 26], see Figure 28
$\theta_{ref}$	293.15	K	determined from
$\lambda_{d,ref}$	2.0153	W m <sup>-1</sup> K <sup>-1</sup>	[42, Table 28],
$A_\lambda$	$-9.8533 \times 10^{-4}$	K <sup>-1</sup>	see Figure 29
$K_{ref}$	$4.0 \times 10^{-20}$	m <sup>2</sup>	–

The concrete of the test specimens (denoted as C60 concrete in [42]) is assumed to be a high strength concrete, class 1 (see [2, Section 6.1] and Section 8), with calcareous aggregates, which can be denoted as "HSC1-C". This classification determines the free thermal strain of concrete and the temperature dependent reduction of its compressive strength according to Eurocode 2 [2], as described in Section 8.

The reference compressive and tensile strengths of concrete at the room temperature is taken from [42, Table 24].

The mass of cement per unit volume of concrete is taken from [42, Table 14].

For the porosity of concrete, the parameters of equation (84) are determined by a linear regression of the data stated in [42, Table 24], see Figure 27.

The density of solid skeleton,  $\rho_s$ , is estimated from the data measured by [42, Table 26]. The corresponding apparent density assumed in our model appears in Figure 28.

The parameters of equation (86) for the thermal conductivity of dry concrete are determined by a linear regression of the data stated in [42, Table 28] (excluding the value for the temperature of 20 °C), see Figure 29 ( $RH = 0$ ). The resulting thermal conductivity of concrete assumed in our model is shown in Figure 29.

The intrinsic permeability of concrete was tested by Mindeguia [42] on concrete samples dried at 80 °C and then heated up to several temperature levels. However, the reference permeability of undamaged concrete at the room temperature is not reported in [42] and hence it is determined by a trial-and-error method in our simulation (cf. [54, p. 277]).

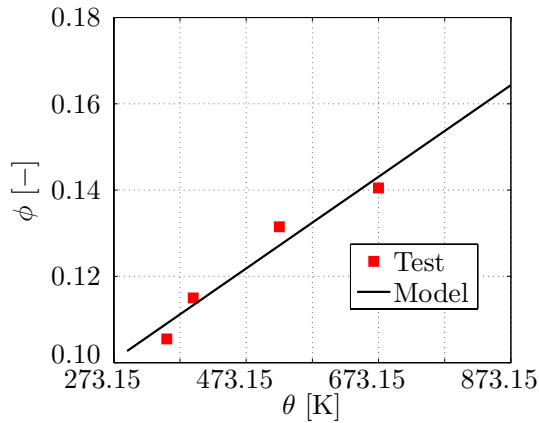


**Figure 27.** Porosity of concrete measured by [42] (points) and assumed in our model (line)

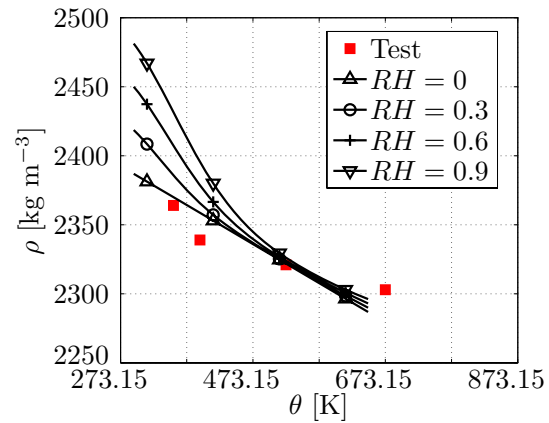


**Figure 28.** Apparent density of concrete measured by [42] (points) and assumed in our model (lines)

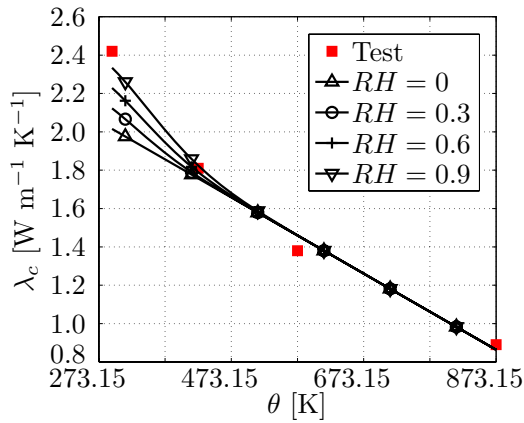


**Figure 29.** Thermal conductivity of concrete measured by [42] (points) and assumed in our model (lines)

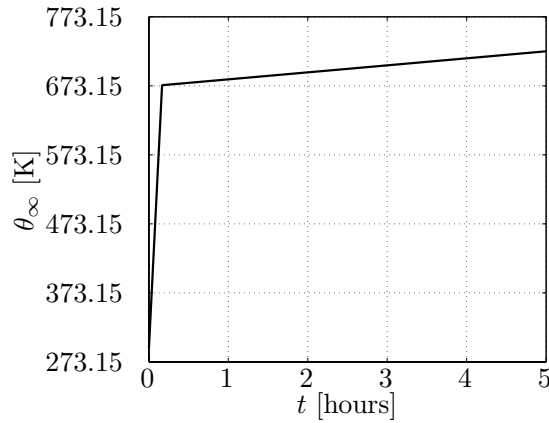


**Figure 30.** Air temperature on the heated side of the specimen used for the simulation of the PTM test 2

The scheme of the analyzed problem, the spatial discretization, the time discretization, and the characteristic time of spalling are identical as in the previous example (see Section 9.1.2).

The initial conditions are assumed as  $P_0 = 1.9194 \times 10^3$  Pa,  $\theta_0 = 293.15$  K,  $\ell_0 = 0.12$  m. For these values, the initial saturation with liquid water  $S_{w,0} = 0.78$ , which is the value reported by Mindeguia [42, Table 18].

The ambient temperature on the heated side,  $\theta_\infty$  [K], has been determined by a

trial-and-error method as (see Figure 30)

$$\theta_{\infty}(t) = \begin{cases} 293.15 + t \frac{380}{300} & \text{for } t \leq 300 \text{ s,} \\ 673.15 + (t - 300) \frac{50}{17700} & \text{for } t > 300 \text{ s,} \end{cases} \quad (116)$$

where  $t$  [s] is the time of heating, and it is practically the same as for the Kalifa's PTM test 1, cf. Figures 16 and 30.

The boundary conditions are summarized in Table 4.

**Table 4.** Boundary conditions parameters for simulation of PTM test 2

Variable	Value		Unit
	Unexposed side	Exposed side	
$P_{\infty}$	$P_0$	$P_0$	Pa
$\theta_{\infty}$	$\theta_0$	$\theta_{\infty}(t)$ , see (116)	K
$\alpha_c$	4	20	$\text{W m}^{-2} \text{K}^{-1}$
$e\sigma$	$0.7 \times 5.67 \times 10^{-8}$	$0.7 \times 5.67 \times 10^{-8}$	$\text{W m}^{-2} \text{K}^{-4}$
$\beta_c$	0.009	0.019	$\text{m s}^{-1}$

*9.2.3. Discussion* The resulting pore pressure and temperature evolutions determined by our simulation are compared with the experimentally measured data in Figures 31, 32 (note that the distances in millimeters stated in the figures are, in accordance with [42], measured from the heated surface). The more detailed illustration of the pore pressure prediction and its comparison with the test data is shown in Figure 33.

From Figures 31–33, it is obvious that also in this case, the present model provides an accurate prediction of the hygro-thermal behaviour of the heated concrete specimen. The spalling behaviour is also simulated correctly since, as mentioned above, during the test, no spalling was observed by Mindeguia [42], which is in accordance with our simulation, see Figure 34 – the maximal value of failure function (31) achieved within the specimen during the test period does not exceeds the value of 1. The evolution of the maximal values of the damage parameter and its components within the specimen during the test period determined by our model is shown in Figure 35.

### 9.3. Simulation of the spalling test

*9.3.1. Experiment description* The spalling experiments were performed by Mindeguia [42] on the  $700 \times 600 \times 120 \text{ mm}^3$  prismatic specimens made of various types of concrete and exposed to various fire scenarios. Hereafter, the spalling test of a high strength concrete (denoted as "B60" in [42]) sample (conditioned in "Air\_2" according to [42]) heated by the ISO 834 fire (in the 150-mm direction) for 60 minutes. This test was duplicated and the data from the both measurements of the spalling depths are stated in [42]. The specimen was placed on the top of the furnace and it was exposed to heating

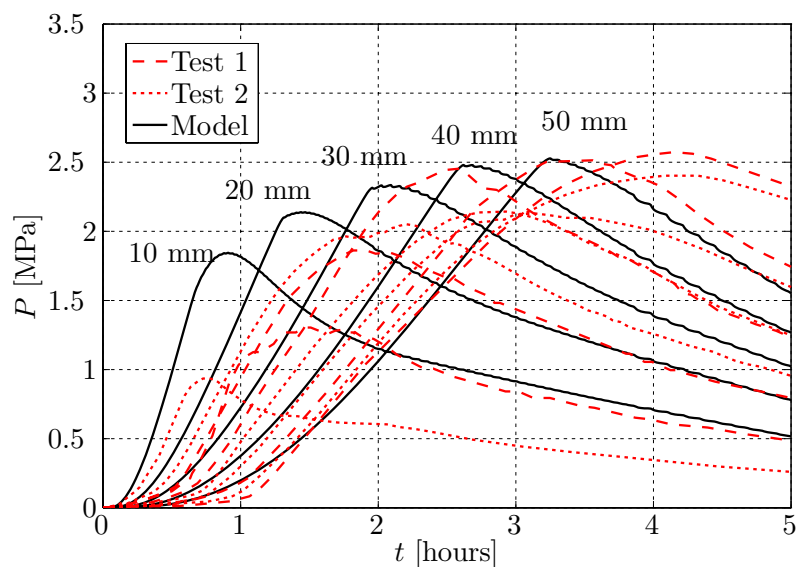


**Figure 31.** Pore pressure evolution measured by [42, Figure 154c] (dashed lines, dotted lines) and determined by the present model (solid lines)

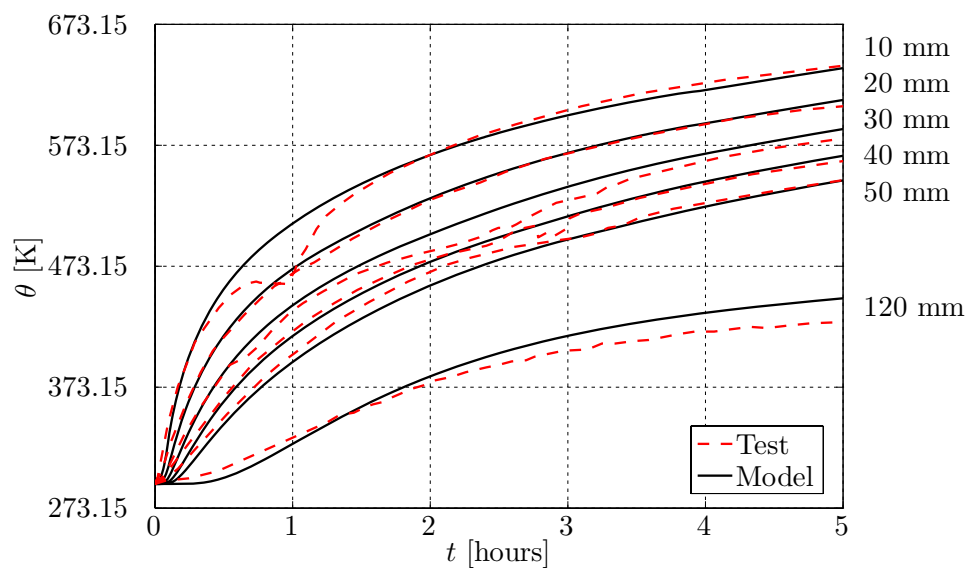


**Figure 32.** Temperature evolution measured by [42, Figure 157c] (dashed lines) and determined by the present model (solid lines)

on the area of  $420 \times 600 \text{ mm}^2$  (see [42, Figure 170]). As mentioned by [42, 43], during the test, the specimen was not subjected to any mechanical load.

Within the test, the temperature and the pore pressure propagations through the specimen were recorded. After the termination of heating, the spalling depths on the

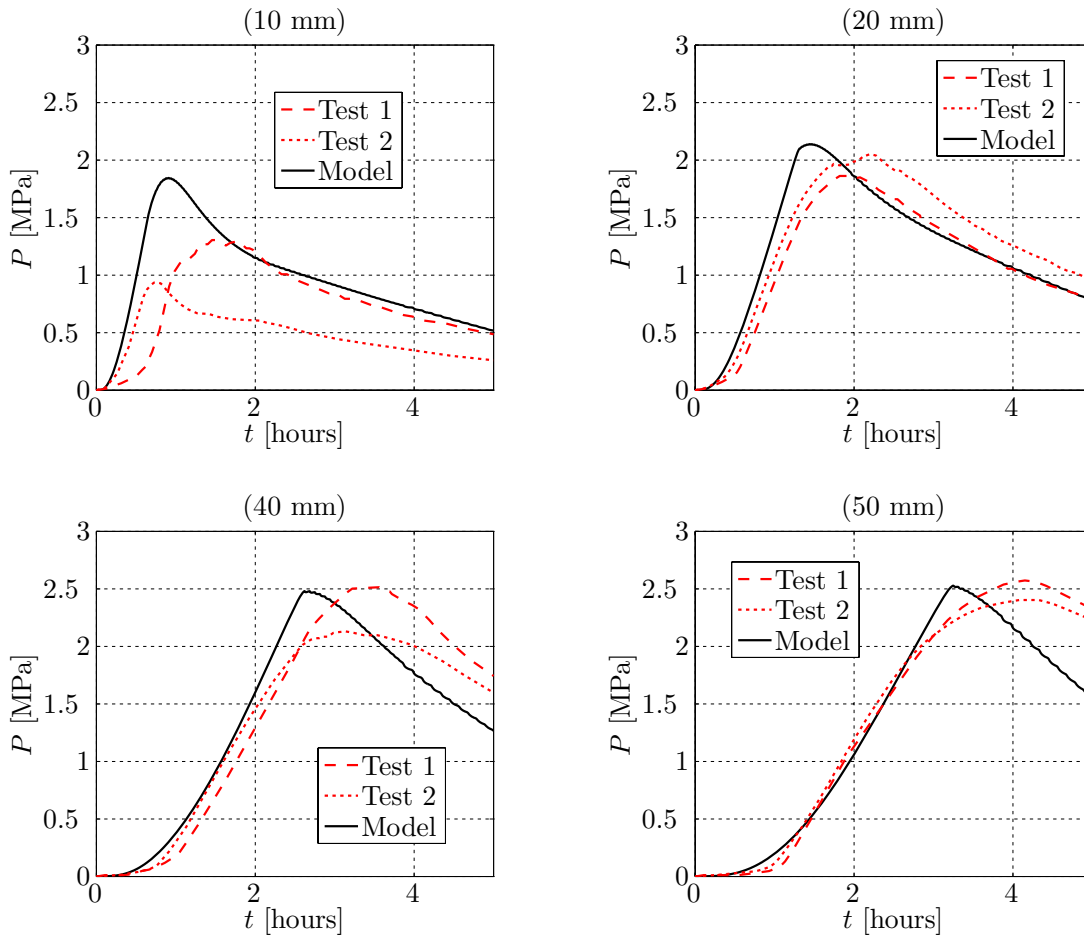


**Figure 33.** Pore pressure evolution measured by [42, Figure 157c] and determined by the present model at the depth of (10, 20, 40, 50) mm from the heated surface

exposed surface were closely measured which enables to determine the maximal and average depths of spalling and depict the well-arranged ”spalling maps”, see [42, 43].

The detailed description of the spalling experiments performed by Mindeguia can be found in [42, 43].

*9.3.2. Modelling* The thermal and hygral properties of the B60 concrete as well as its hygro-thermal behaviour are described in Section 9.2.2.

Scheme of the analyzed problem is displayed in Figure 36. The spatial discretization is performed with the use of linear 1-D elements. In total, 160 elements are employed – 40 elements in the interval  $x \in (0, \ell/2)$ , 40 elements for  $x \in (\ell/2, 3\ell/4)$  and 80 elements in the interval  $x \in (3\ell/4, \ell)$ . For the time discretization as well for the characteristic time of spalling, three values are assumed:  $\Delta t = 1$  s,  $\Delta t = 0.5$  s,  $\Delta t = 0.1$  s, and  $\gamma = 1$  s,  $\gamma = 10$  s, and  $\gamma = 100$  s, respectively, which leads to 9 numerical experiments discussed in Section 9.3.3.

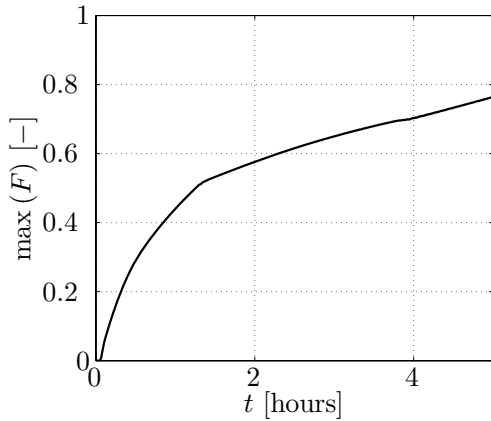


**Figure 34.** Evolution of the failure parameter

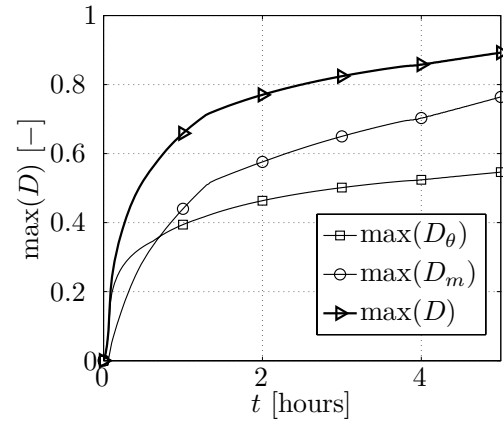


**Figure 35.** Evolution of the damage parameter

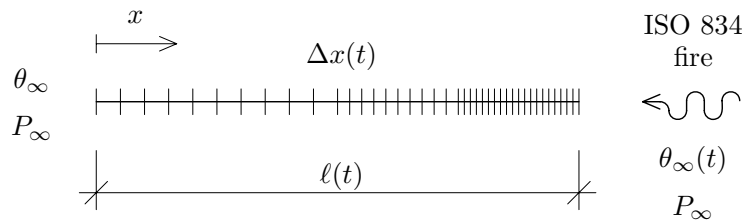


**Figure 36.** Scheme of the analyzed problem

The initial conditions are assumed as  $P_0 = 1.9194 \times 10^3$  Pa,  $\theta_0 = 293.15$  K,  $\ell_0 = 0.15$  m. For these values, the initial saturation with liquid water  $S_{w,0} = 0.78$ , which is the average value of the two initial saturations reported by Mindeguia [42, Table 20].

The ambient temperature on the heated side is governed by the ISO 834 fire curve

$$\theta_\infty(t) = 293.15 + 345 \log(8t + 1), \quad (117)$$

where  $t$  [minutes] is the time of heating.

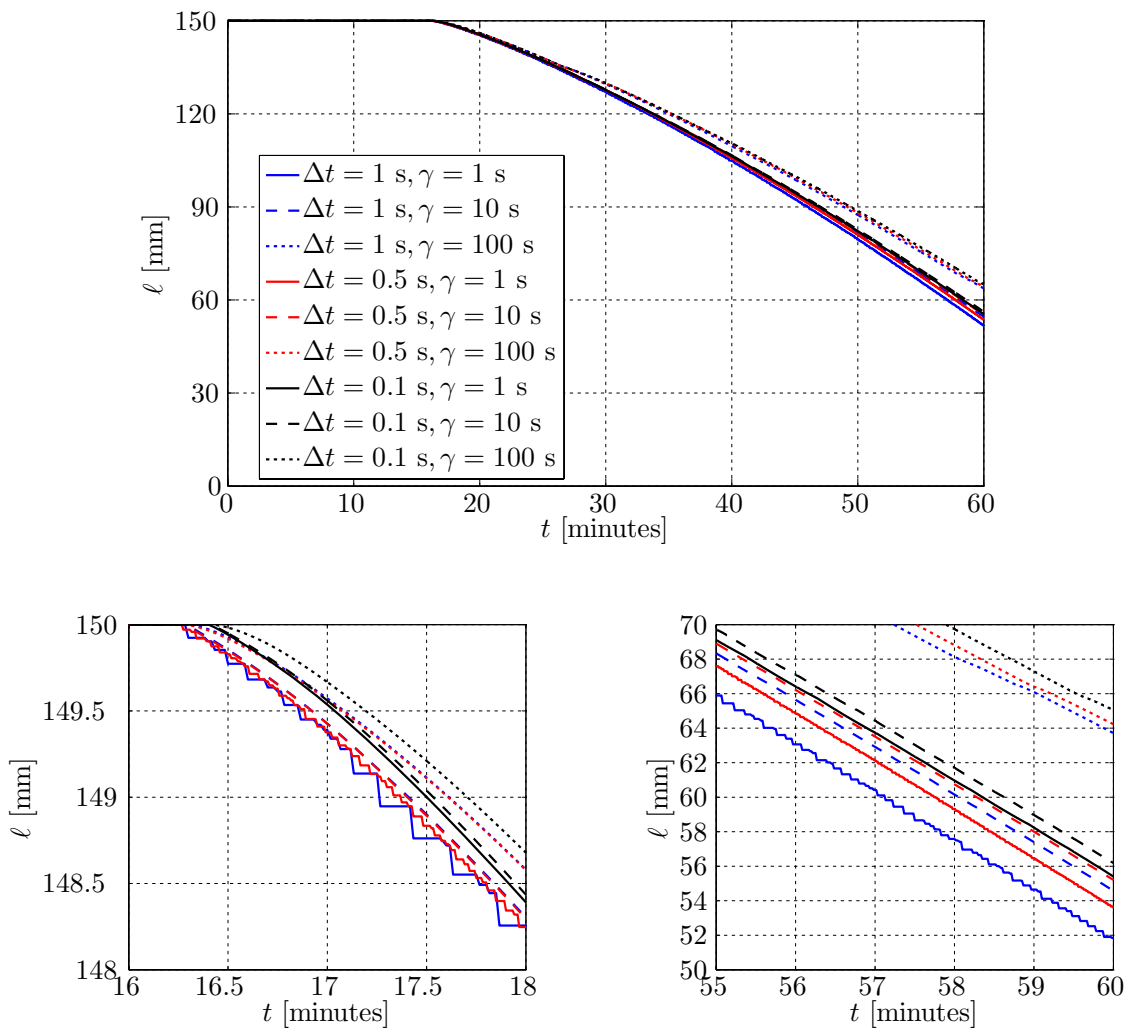
The boundary conditions are summarized in Table 5.

**9.3.3. Discussion** In this case, the spalling of concrete occurred during the test, which is also correctly simulated by the present model. The reduction of the specimen thickness obtained by the calculations is shown in Figure 37.

It is obvious that the model predicted a large amount of concrete spalling – the spalling depth at the end of heating reaches the values from 85 mm to 99 mm, depending on  $\Delta t$  and  $\gamma$  assumed for the calculation. These values of spalling depths are about 2.5 to 4 times as high as measured by Mindeguia – in [42, Table 36] the maximal spalling depths of 34 mm and 23 mm for the first and for the second test are reported, respectively. This

**Table 5.** Boundary conditions parameters for simulation of spalling test

Variable	Value		Unit
	Unexposed side	Exposed side	
$P_\infty$	$P_0$	$P_0$	Pa
$\theta_\infty$	$\theta_0$	$\theta_\infty(t)$ , see (117)	K
$\alpha_c$	4	25	$\text{W m}^{-2} \text{K}^{-1}$
$e\sigma$	$0.7 \times 5.67 \times 10^{-8}$	$0.7 \times 5.67 \times 10^{-8}$	$\text{W m}^{-2} \text{K}^{-4}$
$\beta_c$	0.009	0.019	$\text{m s}^{-1}$

**Figure 37.** Reduction of the specimen thickness due to concrete spalling for the analyzed experiment [42] obtained by the present model

overestimation of the specimen thickness reduction is probably caused by the assumption adopted in the model that the specimen is fully mechanically restrained in the plane perpendicular to its thickness. In the investigated experiment, the only restraint arose

from the fixing the heated concrete by the unheated lateral parts and upper layers of the specimen. It should be noted that the overestimation of the spalling process has been supposed since the assumption of the fully restrained conditions is generally considered as conservative. Moreover, in the real conditions, the structure usually is mechanically restrained and hence, in such a case, the model can provide more accurate prediction.

Numerical experiments demonstrate a computational stability of the present model. From Figure 37, it is obvious that the model is not extremely sensitive on the value of time step. It is also evident that by increasing the characteristic time of spalling as well as by decreing the time step, the spalling proces becomes smoother.

For illustration, the spatial and time distributions of the primary unknowns of the present model are shown in Figure 38.

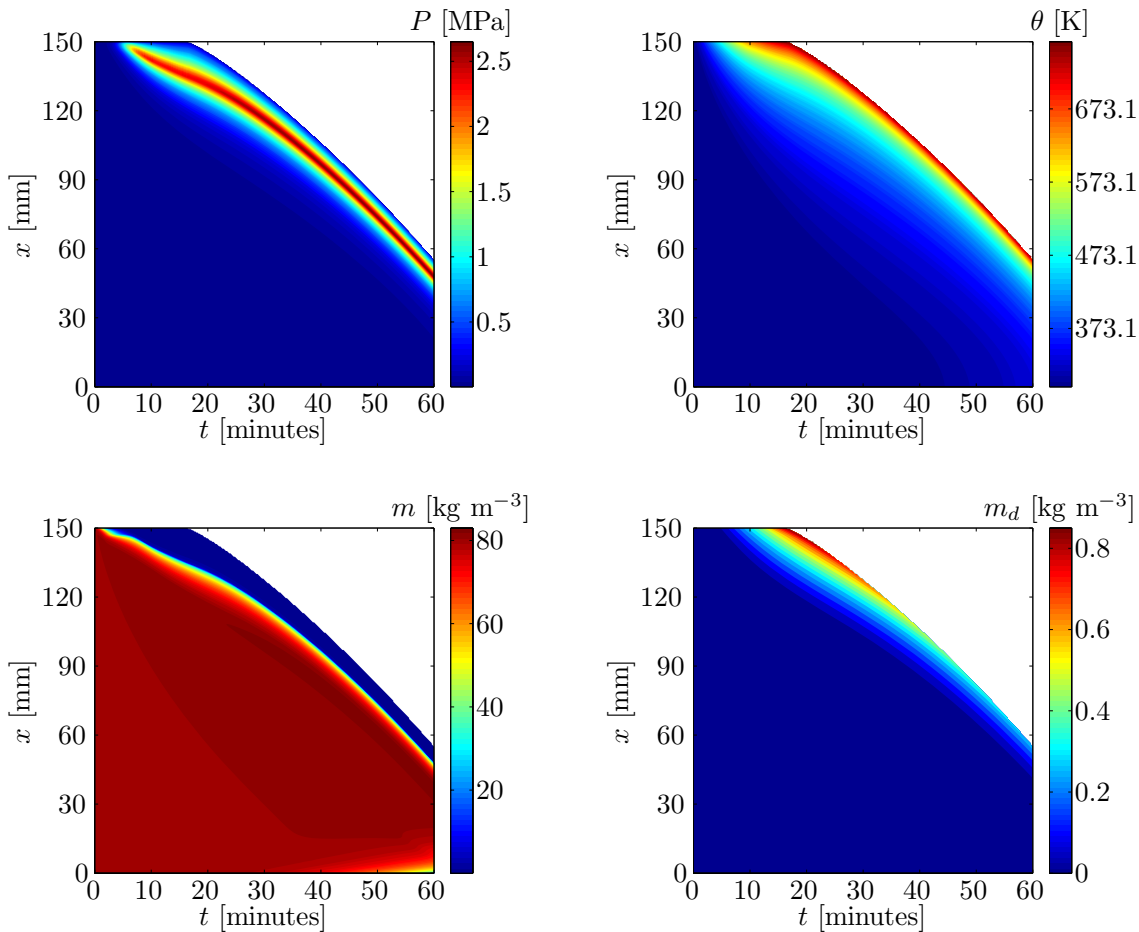


**Figure 38.** Spatial and time distribution of the primary unknowns for the analyzed experiment [42] obtained by the present model (for  $\Delta t = 0.1$  s and  $\gamma = 1$  s)

## 10. Conclusions

In the paper, we proposed a one-dimensional coupled model for simulation of hygro-thermo-mechanical behaviour of concrete walls exposed to high temperatures including the prediction of concrete spalling. The transport-processes-related part of the model was derived from the multi-phase formulations of the laws of conservation of mass and energy. Based on the detailed quantitative parameter analysis, the less important transport phenomena were neglected in order to obtain a simplified but still robust and realistic model of transport processes in heated concrete, which can be expressed in terms of relatively small number of material parameters that can be easily obtained from material tests. The main simplifications employed in our approach consisted in (i) neglecting the diffusive mass flux of water vapour, (ii) removing the separate term describing the effect of diffusion of adsorbed water and including this effect into the liquid water relative permeability,  $K_L$ , and (iii) ignoring the effects of variations of pressure of dry air. The permeability of concrete was supposed to be influenced both by the thermal and mechanical damage of the material, which can be expressed by a multiplicative total damage parameter.

The spalling of concrete was assumed to be caused by a combination of the hygro-thermal stress due to the pore pressure build-up and the thermo-mechanical stress resulting from the restrained thermal dilatation. We employed a simplified mechanical approach based on the assumption that the wall is fully mechanically restrained and the effects of stresses resulting from the external mechanical load as well as the self-weight of the wall on the potential spalling are neglected. An evolution law for moving boundary due to spalling was proposed. It enables to simulate the instantaneous spalling of concrete as a continuous process, which contributes to the computational stability of the numerical solution.

For the model represented by a system of partial differential equations and appropriate boundary and initial conditions, the finite element discretization in space and the semi-implicit discretization in time were employed. The resulting numerical algorithm was incorporated into an in-house MATLAB code that was applied for numerical experiments in order to validate the present model.

The validity of the model was verified by comparing the results obtained by the numerical simulations with the data measured within real high-temperature experiments. Two types of tests were investigated – the tests of hygro-thermal behaviour of high-strength concrete specimens  $300 \times 300 \times 120 \text{ mm}^3$  heated by a radiant heater of temperature of  $600 \text{ }^\circ\text{C}$  performed by Kalifa *et al.* [35] and Mindeguia [42] and the spalling test of high-strength concrete specimens  $700 \times 600 \times 120 \text{ mm}^3$  exposed to the ISO 834 fire performed by Mindeguia [42]. All the material properties assumed for the simulations, except the reference intrinsic permeability of undamaged concrete at the room temperature,  $K_{ref}$ , were adopted from the data measured by Kalifa *et al.* [35] and Mindeguia [42], respectively. The values of  $K_{ref}$  were not reported by the authors of the tests (Kalifa *et al.* [35] and Mindeguia [42] reported only the values of the intrinsic

permeability dried at 105 °C or 80 °C, respectively, and then heated up to several temperature levels).

By comparing the calculated and measured data, the following findings can be drawn:

- the model is able to simulate the hygro-thermal behaviour of heated concrete on an appropriate level of accuracy, the temperature and pore pressure distributions obtained by the present model are in close agreement with the data measured by Kalifa *et al.* [35] and Mindeguia [42];
- for the investigated examples, the model provided a correct qualitative prediction of concrete spalling (whether it occurred or not);
- the quantitative prediction of spalling for the Mindeguia's [42] spalling test was overestimated (the values of spalling depths determined by the model at the end of the test period are about 2.5 to 4 times as high as measured by Mindeguia [42]), which is probably due to the assumption of the fully mechanical restraint of the specimen adopted in the model that is however not fulfilled in the investigated test setup by Mindeguia [42]; it can be supposed that in real structures (with some level of restraint), the model can provide more accurate prediction.

For future research, it could be recommended to focuss on:

- determination of the reference intrinsic permeability of undamaged concrete at the room temperature;
- validation of the present model on a real structure exposed to fire or on the results of full-scale fire experiments;
- extension of the present model for two-dimensional problems and improve the mechanical part of the model in order to describe various types of loading and restrain conditions.

## Appendix A. Physical mechanisms of transport processes in concrete at high temperatures

In this Appendix we address, on the quantitative level, contributions of different transport mechanisms in concrete exposed to ambient high-temperatures. To this goal, we will first summarize modelling assumptions and state variables employed in the derivation of complete multi-phase formulations, together with the dependence of material constants on the state variables. Then, by expressing the thermodynamic fluxes in terms of the same state variables, we will obtain closed-form expressions for the corresponding transport coefficients. Their relative importance will be evaluated at the level of material point and these results will allow us to explore the domains of applicability and the connection of the presented simplified model against detailed multi-phase descriptions.

## Appendix B. Nomenclature

Symbol	Units	Description
$\alpha_c$	$[\text{W m}^{-2} \text{K}^{-1}]$	convective heat transfer coefficient
$\beta_c$	$[\text{m s}^{-1}]$	convective mass transfer coefficient
$\epsilon_{tot}$	$[-]$	total strain
$\epsilon_\theta$	$[-]$	free thermal strain
$\epsilon_\sigma$	$[-]$	instantaneous stress-related strain
$\epsilon_{cr}$	$[-]$	creep strain
$\epsilon_{tr}$	$[-]$	transient strain
$\eta_s$	$[-]$	volume fraction of the solid microstructure
$\eta_w$	$[-]$	volume fraction of liquid phase
$\eta_g$	$[-]$	volume fraction of gas phase
$\phi$	$[-]$	porosity
$\rho_s$	$[\text{kg m}^{-3}]$	density of the solid microstructure
$\rho_g$	$[\text{kg m}^{-3}]$	gas phase density
$\rho_a$	$[\text{kg m}^{-3}]$	dry air phase density
$\rho_v$	$[\text{kg m}^{-3}]$	vapour phase density
$\rho_{v\infty}$	$[\text{kg m}^{-3}]$	ambient vapour phase density
$\rho_w$	$[\text{kg m}^{-3}]$	liquid phase density
$\mu_w$	$[\text{Pa s}]$	liquid water dynamic viscosity
$\mu_g$	$[\text{Pa s}]$	gas dynamic viscosity
$\sigma$	$[\text{Pa}]$	stress
$\sigma_{ht}$	$[\text{Pa}]$	stress caused by hygro-thermal processes
$\sigma_{tm}$	$[\text{Pa}]$	stress caused by thermo-mechanical processes
$\sigma_{SB}$	$[\text{W m}^{-2} \text{K}^{-1}]$	Stefan-Boltzmann constant
$\theta$	$[\text{K}]$	absolute temperature
$\theta_\infty$	$[\text{K}]$	ambient absolute temperature

$\lambda_c$	$[\text{W m}^{-1} \text{K}^{-1}]$	effective thermal conductivity of moist concrete
$\tau$	$[\text{s}]$	characteristic time of mass loss governing the asymptotic evolution of the dehydration process
$c$	$\text{kg m}^{-3}$	mass of cement per $\text{m}^3$ of concrete
$c_p^w$	$[\text{J kg}^{-1} \text{K}^{-1}]$	specific heat at constant pressure of liquid water
$c_p^v$	$[\text{J kg}^{-1} \text{K}^{-1}]$	specific heat at constant pressure of water vapour
$c_p^a$	$[\text{J kg}^{-1} \text{K}^{-1}]$	specific heat at constant pressure of dry air
$c_p^s$	$[\text{J kg}^{-1} \text{K}^{-1}]$	specific heat at constant pressure of solid phase
$c_p^g$	$[\text{J kg}^{-1} \text{K}^{-1}]$	specific heat at constant pressure of gas mixture
$e$	$[-]$	emissivity of the interface
$f_c$	$[\text{Pa}]$	uniaxial compressive strength of concrete
$f_t$	$[\text{Pa}]$	uniaxial tensile strength of concrete
$F$	$[-]$	failure function
$h_e$	$[\text{J kg}^{-1}]$	enthalpy of evaporation per unit mass
$h_d$	$[\text{J kg}^{-1}]$	enthalpy of dehydration per unit mass
$H^w$	$[\text{J kg}^{-1}]$	specific enthalpy of liquid water
$H^v$	$[\text{J kg}^{-1}]$	specific enthalpy of water vapour
$H^s$	$[\text{J kg}^{-1}]$	specific enthalpy of chemically bound water
$\mathbf{J}_w$	$[\text{kg m}^{-2} \text{s}^{-1}]$	liquid water mass flux
$\mathbf{J}_v$	$[\text{kg m}^{-2} \text{s}^{-1}]$	water vapour mass flux
$\mathbf{J}_M$	$[\text{kg m}^{-2} \text{s}^{-1}]$	moisture flux
$K$	$[\text{m}^2]$	intrinsic permeability
$K_{rw}$	$[-]$	relative permeability of liquid water
$K_{rg}$	$[-]$	relative permeability of gas
$\ell$	$[\text{m}]$	thickness of a concrete wall
$m_d$	$[\text{kg m}^{-3} \text{s}^{-1}]$	mass source term related to the dehydration process
$m_{d,eq}$	$[\text{kg m}^{-3} \text{s}^{-1}]$	mass of water released at the equilibrium
$m_e$	$[\text{kg m}^{-3} \text{s}^{-1}]$	vapour mass source caused by the liquid water evaporation
$M_w$	$[\text{kg kmol}^{-1}]$	molar mass of liquid water
$M_a$	$[\text{kg kmol}^{-1}]$	molar mass of dry air
$P$	$[\text{Pa}]$	pore pressure due to water vapour ( $P = P_v$ )
$P_c$	$[\text{Pa}]$	capillary pressure
$P_v$	$[\text{Pa}]$	water vapour pressure
$P_a$	$[\text{Pa}]$	dry air pressure
$P_g$	$[\text{Pa}]$	gas pressure
$P_L$	$[\text{Pa}]$	pressure of liquid water
$P_s$	$[\text{Pa}]$	water vapour saturation pressure
$q_c$	$[\text{W m}^{-2}]$	heat flux vector
$R$	$[\text{J kmol}^{-1} \text{K}^{-1}]$	gas constant
$RH$	$[-]$	relative humidity ( $RH = P_v/P_s$ )
$S_w$	$[-]$	degree of saturation with liquid water
$S_B$	$[-]$	degree of saturation with adsorbed water

$S_{ssp}$	$[-]$	solid saturation point
$v_g$	$[\text{m s}^{-1}]$	velocity of gaseous phase
$v_w$	$[\text{m s}^{-1}]$	velocity of liquid phase
$v_a$	$[\text{m s}^{-1}]$	velocity of dry air
$v_v$	$[\text{m s}^{-1}]$	velocity of vapour

*Acknowledgement.* This research has been supported by the Czech Science Foundation, project GAČR 13-18652S (the first and the second author), and by the Grant Agency of the Czech Technical University in Prague, project SGS13/038/OHK1/1T/11 (the second author). The support is gratefully acknowledged.

## References

- [1] *Eurocode 2: Design of concrete structures – Part 1-1: General rules and rules for buildings*. CEN, 2004.
- [2] *Eurocode 2: Design of concrete structures – Part 1-2: General rules – Structural fire design*. CEN, 2004.
- [3] A. Alnajim. *Modelisation et simulation du comportement du beton sous hautes temperatures par une approche thermo-hygro-mecanique couplee. Application a des situations accidentelles*. PhD thesis, Universite de Merne la Vallee, 2004.
- [4] Y. Anderberg. The impact of various material models on structural fire behaviour prediction. In K.H. Tan, V.K.R. Kodur, and T.H. Tan, editors, *Proceedings of the Fifth International Conference on Structures in Fire (SiF'08)*, pages 253–265, Singapore, 2008. Nanyang Technological University.
- [5] Y. Anderberg and S. Thelandersson. *Stress and deformation characteristics of concrete at high temperatures. 2. Experimental investigation and material behaviour model*. Lund Institute of Technology, 1976.
- [6] Z.P. Bažant, J.-Ch. Chern, and W. Thonguthai. Finite element program for moisture and heat transfer in heated concrete. *Nucl. Eng. Des.*, 68(1):61–70, 1981.
- [7] Z.P. Bažant and W. Thonguthai. Pore pressure and drying of concrete at high temperature. *Proc. ASCE, J. Eng. Mech. Div.*, 104(5):1059–1079, 1978.
- [8] Z.P. Bažant and W. Thonguthai. Pore pressure in heated concrete walls: theoretical prediction. *Mag. Concr. Res.*, 31(107):67–76, 1979.
- [9] M. Beneš, R. Štefan, and J. Zeman. Analysis of coupled transport phenomena in concrete at elevated temperatures. *Appl. Math. Comput.*, 219:7262–7274, 2013.
- [10] S. Bratina, B. Čas, M. Saje, and I. Planinc. Numerical modelling of behaviour of reinforced concrete columns in fire and comparison with eurocode 2. *International J. Solids Struct.*, 42(21-22):5715 – 5733, 2005.
- [11] J.V. Carstensen. Material modelling of reinforced concrete at elevated temperatures. Master's thesis, Technical University of Denmark, 2011.
- [12] J.H. Chung and G.R. Consolazio. Numerical modeling of transport phenomena in reinforced concrete exposed to elevated temperatures. *Cement Concrete Res.*, 35(3):597–608, 2005.
- [13] S. Dal-Pont and A. Ehrlacher. Numerical and experimental analysis of chemical dehydration, heat and mass transfers in a concrete hollow cylinder submitted to high temperatures. *Int. J. Heat Mass Tran.*, 47(1):135–147, 2004.
- [14] C.T. Davie, C.J. Pearce, and N. Bićanić. Coupled heat and moisture transport in concrete at elevated temperatures-effects of capillary pressure and adsorbed water. *Numer. Heat Tr. A-Appl.*, 49(8):733–763, 2006.
- [15] C.T. Davie, C.J. Pearce, and N. Bićanić. A fully generalised, coupled, multi-phase, hygro-thermo-mechanical model for concrete. *Mater. Struct.*, 43(1):13–33, 2010.
- [16] C.T. Davie, C.J. Pearce, and N. Bićanić. Aspects of permeability in modelling of concrete exposed to high temperatures. *Transport Porous Med.*, 95(3):627–646, 2012.
- [17] M.B. Dwaikat and V.K.R. Kodur. Hydrothermal model for predicting fire-induced spalling in concrete structural systems. *Fire Safety J.*, 44(3):425–434, 2009.
- [18] J.H.H. Fellingner. *Shear and anchorage behaviour of fire exposed hollow core slabs*. PhD thesis, TU Delft, 2004.
- [19] A. Feraille-Fresnet, P. Tamagny, A. Ehrlacher, and J. Sercombe. Thermo-hydro-chemical modelling of a porous medium submitted to high temperature: An application to an axisymmetrical structure. *Math. Comput. Model.*, 37(5):641–650, 2003.
- [20] D.J. Furbish. *Fluid Physics in Geology. An Introduction of Fluid Motions on Earth's Surface and Within Its Crust*. Oxford University Press, 1997.
- [21] D. Gawin, C.E. Majorana, and B.A. Schrefler. Numerical analysis of hygro-thermal behaviour

- and damage of concrete at high temperature. *Mech. Cohes.-Frict. Mat.*, 4(1):37–74, 1999.
- [22] D. Gawin and F. Pesavento. An overview of modeling cement based materials at elevated temperatures with mechanics of multi-phase porous media. *Fire Technol.*, 48(3):753–793, 2012.
- [23] D. Gawin, F. Pesavento, and B.A. Schrefler. Modelling of hygro-thermal behaviour and damage of concrete at temperature above the critical point of water. *Int. J. Numer. Anal. Met.*, 26(6):537–562, 2002.
- [24] D. Gawin, F. Pesavento, and B.A. Schrefler. Modelling of hygro-thermal behaviour of concrete at high temperature with thermo-chemical and mechanical material degradation. *Comput. Methods Appl. Mech. Engrg.*, 192(13-14):1731–1771, 2003.
- [25] D. Gawin, F. Pesavento, and B.A. Schrefler. Towards prediction of the thermal spalling risk through a multi-phase porous media model of concrete. *Comput. Methods Appl. Mech. Engrg.*, 195(41-43):57075729, 2006.
- [26] D. Gawin, F. Pesavento, and B.A. Schrefler. What physical phenomena can be neglected when modelling concrete at high temperature? A comparative study. Part 1: Physical phenomena and mathematical model. *Int. J. Solids Struct.*, 48(13):1927–1944, 2011.
- [27] D. Gawin, F. Pesavento, and B.A. Schrefler. What physical phenomena can be neglected when modelling concrete at high temperature? A comparative study. Part 2: Comparison between models. *Int. J. Solids Struct.*, 48(13):1945–1961, 2011.
- [28] T. Gernay and J.-M. Franssen. Consideration of transient creep in the eurocode constitutive model for concrete in the fire situation. In V.K.R. Kodur and J.-M. Franssen, editors, *Proceedings of the Sixth International Conference Structures in Fire*, pages 784–791, Lancaster, PA, 2010. DEStech Publications.
- [29] Z. He and Y. Song. Failure mode and constitutive model of plain high-strength high-performance concrete under biaxial compression after exposure to high temperatures. *Acta Mech. Solida Sin.*, 21(2):149–159, 2008.
- [30] Y. Ichikawa and G.L. England. Prediction of moisture migration and pore pressure build-up in concrete at high temperatures. *Nucl. Eng. and Des.*, 228(1-3):245–259, 2004.
- [31] R. Jansson and L. Boström. The influence of pressure in the pore system on fire spalling of concrete. *Fire Technol.*, 46(1):217–230, 2010.
- [32] M. Jirásek and Z.P. Bažant. *Inelastic Analysis of Structures*. Wiley, 2002.
- [33] J.W. Ju and Y. Zhang. A thermomechanical model for airfield concrete pavement under transient high temperature loadings. *Int. J. Damage Mech.*, 7(1):24–46, 1998.
- [34] P. Kalifa, G. Chene, and Ch. Galle. High-temperature behaviour of hpc with polypropylene fibres: From spalling to microstructure. *Cement Concrete Res.*, 31(10):1487–1499, 2001.
- [35] P. Kalifa, F.D. Menneteau, and D. Quenard. Spalling and pore pressure in hpc at high temperatures. *Cement Concrete Res.*, 30(12):1915–1927, 2000.
- [36] P. Kalifa, M. Tsimbrovska, and V. Baroghel-Bouny. High-performance concrete at elevated temperatures – an extensive experimental investigation of thermal and hygral properties and microstructure. In P.-C. Aïtcin and Y. Delagrave, editors, *International Symposium on High-Performance and Reactive Powder Concretes*, pages 259–279, Sherbrooke, Canada, 1998. Université de Sherbrooke.
- [37] A. Houry and Y. Anderberg. *Fire safety design – Concrete spalling review*. Swedish National Road Administration, 2000.
- [38] K. Kukla. *Concrete at high temperatures – Hygro-thermo-mechanical degradation of concrete*. PhD thesis, University of Glasgow, 2010.
- [39] L.Y. Li and J. Purkiss. Stress–strain constitutive equations of concrete material at elevated temperatures. *Fire Saf. J.*, 40(7):669 – 686, 2005.
- [40] P. Majumdar, A. Gupta, and A. Marchertas. Moisture propagation and resulting stress in heated concrete walls. *Nucl. Eng. Des.*, 156(1-2):147–158, 1995.
- [41] P. Menétrey and K.J. Willam. Triaxial failure criterion for concrete and its generalization. *ACI Struct. J.*, 92(3):311–318, 1995.

- [42] J.-C. Mindeguia. *Contribution expérimentale a la compréhension des risques d'instabilité thermique des bétons*. PhD thesis, UPPA, 2009.
- [43] J.-C. Mindeguia, P. Pimienta, H. Carré, and C. La Borderie. Experimental analysis of concrete spalling due to fire exposure. *Eur. J. Environ. Civ. En.*, 17(6):453–466, 2013.
- [44] J.-C. Mindeguia, P. Pimienta, A. Noumowé, and M. Kanema. Temperature, pore pressure and mass variation of concrete subjected to high temperature – experimental and numerical discussion on spalling risk. *Cem. Concr. Res.*, 40(3):477–487, 2010.
- [45] Y. Msaad. Comparison between hydraulic and thermal spalling in heated concrete based on numerical modeling. *J. Eng. Mech.*, 133(6):608615, 2007.
- [46] D.J. Naus. A compilation of elevated temperature concrete material property data and information for use in assessments of nuclear power plant reinforced concrete structures. Technical report, Office of Nuclear Regulatory Research, 2010.
- [47] F. Pesavento. *Non-linear modelling of concrete as multiphase porous material in high temperature conditions*. PhD thesis, Università degli Studi di Padova, 2000.
- [48] M.T. Phan. *Modélisation explicite de l'écaillage sous incendie du béton: Approche thermo-hydro-mécanique avec des conditions aux limites évolutives*. PhD thesis, Université Paris-Est, 2012.
- [49] J.N. Reddy. *An Introduction to Nonlinear Finite Element Analysis*. Oxford University Press, USA, 2004.
- [50] B.A. Schrefler, P. Brunello, D. Gawin, C.E. Majorana, and F. Pesavento. Concrete at high temperature with application to tunnel fire. *Comput. Mech.*, 29(1):43–51, 2002.
- [51] M. Shekarchi, G. Debicki, Y. Billard, and L. Coudert. Heat and mass transfer of high performance concrete for reactor containment under severe accident conditions. *Fire Technol.*, 39(1):63–71, 2003.
- [52] R.T. Tenchev, L.Y. Li, and J.A. Purkiss. Finite element analysis of coupled heat and moisture transfer in concrete subjected to fire. *Numer. Heat Tr. A-Appl.*, 39(7):685–710, 2001.
- [53] M.J. Terro. Numerical modeling of the behavior of concrete structures in fire. *ACI Struct. J.*, 95(2):183–192, 1998.
- [54] A. Witek, D. Gawin, F. Pesavento, and B.A. Schrefler. Finite element analysis of various methods for protection of concrete structures against spalling during fire. *Comput. Mech.*, 39(3):271–292, 2007.
- [55] M. Zeiml, R. Lackner, and H.A. Mang. Experimental insight into spalling behavior of concrete tunnel linings under fire loading. *Acta Geotechnica*, 3(4):295–308, 2008.